

Modifications to the K-Profile Parameterization with Nondiffusive Fluxes for Langmuir Turbulence[¶]

TOMAS CHOR,^a JAMES C. MCWILLIAMS,^a and MARCELO CHAMECKI^a

^a University of California, Los Angeles, Los Angeles, California

(Manuscript received 9 October 2020, accepted 12 January 2021)

ABSTRACT: The *K*-profile parameterization (KPP) is a common method to model turbulent fluxes in regional and global oceanic models. Many versions of KPP exist in the oceanic sciences community, and one of their main differences is how they take the effects of nonbreaking waves into account. Although there is qualitative consensus that nonbreaking waves enhance vertical mixing due to the ensuing Langmuir circulations, there is no consensus on the quantitative aspects and modeling approach. In this paper we use a recently developed method to estimate both components of KPP (the diffusive term, usually called local, and the nondiffusive component, usually called nonlocal) based on numerically simulated turbulent fluxes without any a priori assumptions about their scaling or their shape. Through this method we show that the cubic shape usually used in KPP is not optimal for wavy situations and propose new ones. Furthermore, we show that the formulation for the nondiffusive fluxes, which currently only depend on the presence of surface buoyancy fluxes, should also take wave effects into account. We also investigate how the application of these changes to KPP improves the representation of turbulent fluxes in a diagnostic approach when compared with previous models.

KEYWORDS: Ocean; Ocean dynamics; Waves, oceanic; Oceanic mixed layer; Ocean models

1. Introduction

Many state-of-the-art regional and global models parameterize vertical mixing in ocean surface boundary layers (OSBLs) with the *K*-profile parameterization (KPP; Large et al. 1994), which can be written as

$$\langle w'c' \rangle = \underbrace{-K(z) \frac{\partial \langle C \rangle}{\partial z}}_{F_D(z)} + F_{ND}(z). \quad (1)$$

Here z is the vertical coordinate (negative for the ocean), F_D and F_{ND} are the diffusive and nondiffusive components of the turbulent flux, $K(z)$ is the eddy diffusivity for a passive scalar, w is the vertical velocity of the flow, $\langle C \rangle$ and c' are the average concentration of a passive scalar and its turbulent fluctuation, respectively. A prime denotes a turbulent fluctuation and angle brackets denote a temporal and horizontal average. While KPP is a complete model (providing closure for buoyancy and momentum fluxes), we focus on passive scalars in this paper (for the sake of simplicity in initial investigations), with the general aim of investigating opportunities for improving KPP in wavy regimes.

Currently there exist many different versions of KPP, and they differ in mainly two aspects: their definition of flux profiles [i.e., $K(z)$ and $F_{ND}(z)$] and the calculation of the boundary layer

depth h . Although it has been shown numerically that Langmuir turbulence heavily impacts the determination of h by increased entrainment at the bottom (Grant and Belcher 2009; McWilliams et al. 2014), we focus in this paper only on the determination of KPP profiles and treat h as a given. The reader is directed to the recent study of Li and Fox-Kemper (2017) and references therein for more information on the efforts to calculate h in the presence of Langmuir turbulence.

Efforts at adapting F_D and $F_{ND}(z)$ to Langmuir turbulence mostly focused on changing the magnitude of $K(z)$, and few studies have considered the possibility of Langmuir turbulence directly modifying the shape and magnitude of nondiffusive fluxes F_{ND} (Reichl et al. 2016; Chen et al. 2016). While the formulation of $K(z)$ relative to surface wind shear and surface buoyancy fluxes remain the same throughout different versions¹ [based on Monin–Obukhov similarity theory (MOST)], the effect of nonbreaking waves on the magnitude of $K(z)$ varies significantly from model to model (Li et al. 2019).

While there is general consensus that the presence of non-breaking waves (and therefore Langmuir cells; Thorpe 2004) should enhance the eddy diffusivity of the flow, there is disagreement on the quantitative aspects (Smyth et al. 2002; Takaya et al. 2010; Van Roekel et al. 2012; Li et al. 2019). The fact that many different studies cannot quantitatively agree on the Langmuir-driven enhancement could mean that merely enhancing $K(z)$ is

[¶] Supplemental information related to this paper is available at the Journals Online website: <https://doi.org/10.1175/JPO-D-20-0250.s1>.

Chor's current affiliation: Department of Atmospheric and Oceanic Science, University of Maryland, College Park, College Park, Maryland.

Corresponding author: Marcelo Chamecki, chamecki@ucla.edu

¹ Some exceptions are Sinha et al. (2015), Yang et al. (2015), and Large et al. (2019b). The CVMix project (Griffies et al. 2015) also allows for different shapes.

not an appropriate strategy (Van Roekel et al. 2018; Chamecki et al. 2019). With that in mind, we adopt an alternative approach that takes Langmuir effects into account in both $K(z)$ and $F_{\text{ND}}(z)$.

In the vast majority of previous KPP versions F_{ND} is assumed to (i) have the same shape as the eddy diffusivity² and (ii) to depend only on the surface buoyancy fluxes (implying that F_{ND} is designed to model the action of convective plumes specifically). We relax assumption ii since it has been shown that nondiffusive fluxes are affected by Langmuir cells (Chen et al. 2016; Chamecki et al. 2019) and relax assumption i based on recent results for the atmosphere that suggest that the optimal form for F_{ND} can be different from the cubic function that is commonly used in the literature (Chor et al. 2020b).

To investigate how to improve KPP in the presence of Langmuir turbulence, we use the method developed in Chor et al. (2020b). This optimization-based method uses the asymmetry in the vertical transport of two independent scalars (i.e., the fact that scalars introduced at the surface are transported more efficiently than scalars entrained at the bottom of the boundary layer; Wyngaard and Brost 1984) to bound the transport carried by the diffusive component and is capable of systematically estimating profiles for F_D [therefore $K(z)$] and $F_{\text{ND}}(z)$ without any imposed shape or scaling. Therefore, the main advantage of this method is that it has few assumptions and the shapes and magnitudes of $K(z)$ and $F_{\text{ND}}(z)$ are dictated by the data, as opposed to being a function of scalings chosen a priori.

We use results for $K(z)$ and $F_{\text{ND}}(z)$ obtained with the optimization method to investigate the separation between nondiffusive and diffusive fluxes of passive scalars in several numerically simulated OSBL regimes ranging from waveless neutral to combinations of surface buoyancy fluxes and different types of waves. We then use the results to investigate modifications to the KPP formulation [both $K(z)$ and $F_{\text{ND}}(z)$ separately] in a way that is optimized for wavy regimes. We consider our main contributions to be the systematic assessment that Langmuir effects are required to be considered in the formulation of nondiffusive fluxes and the investigation of different shapes for KPP profiles.

We note that our goal is not to introduce a full model, but to investigate how changes in the formulation of KPP can lead to a model for passive scalar mixing that is better suited for regimes with waves. While the focus of this work lies in passive scalars, we briefly present selected results for temperature following the same modeling used for the tracers in section 6. For the sake of convenience, a list of the main symbols used in this paper is included in Table 1.

2. Theoretical aspects and definitions

a. Definitions

Since it is up for debate whether F_D and F_{ND} represent the turbulent vertical fluxes due to local and nonlocal processes (Zhou et al. 2018), we refer to the first and second terms on the right-hand side of Eq. (1) (viz., F_D and F_{ND}) as diffusive and nondiffusive.

² The notable exception is CVMix (Griffies et al. 2015), which allows different shapes.

TABLE 1. List of main symbols used in this paper roughly organized by order of appearance. Note that all concentrations used in this paper are normalized by arbitrary units. The angle-bracket operator is implemented as a horizontal and time average.

Symbol	Description	Units
$\langle v' c' \rangle$	Vertical turbulent flux of scalar C	m s^{-1}
$\langle v' c' \rangle_s$	Surface vertical flux of scalar C	m s^{-1}
$\langle v' c' \rangle_e$	Vertical turbulent flux of scalar C at entrainment	m s^{-1}
$\partial \langle C \rangle / \partial z$	Average vertical gradient of scalar C	m^{-1}
H	OSBL depth	m
Σ	Normalized vertical coordinate (z/h)	—
$K(\sigma)$	Eddy diffusivity for a passive scalar	$\text{m}^2 \text{s}^{-1}$
$F_D(\sigma)$	Diffusive component of the vertical turbulent flux	m s^{-1}
$F_{\text{ND}}(\sigma)$	Nondiffusive component of the vertical turbulent flux	m s^{-1}
La_t	Turbulent Langmuir number [Eq. (2)]	—
La_{SL}	Surface-layer Langmuir number [Eq. (3)]	—
Λ	Stability parameter [Eq. (4)]	—
$u_s(\sigma)$	KPP velocity scale [Eq. (6)]	m s^{-1}
u_*	Friction velocity	m s^{-1}
$G_k(\sigma)$	Nondimensional shape function for $K(\sigma)$	—
$G_s(\sigma)$	Nondimensional shape function for surface-driven nondiffusive fluxes	—
$G_e(\sigma)$	Nondimensional shape function for entrainment-driven nondiffusive fluxes	—
$G_n(\sigma)$	Cubic nondimensional shape function [Eq. (8)]	—
$G_i(\sigma)$	Shape function for surface-driven nondiffusive fluxes diagnosed from wavy regimes	—
$G_j(\sigma)$	Averaged normalized eddy diffusivity for wavy regimes	—
$g_s(\sigma)$	Base nondimensional function for $G_s(\sigma)$ [Eq. (15)]	—
ε	Langmuir enhancement parameter	—
ε^{sc}	Langmuir enhancement parameter fitted for the surface layer	—
$\varepsilon^{\text{OSBL}}$	Langmuir enhancement parameter fitted for the entire OSBL	—
χ	Cost function for optimization procedure [Eq. (11)]	—
R_F	Approximate ratio of nondiffusive to total fluxes [Eq. (12)]	—
δF	Mean normalized flux error in the OSBL [Eq. (18)]	—

We define two different passive tracers that will be useful in implementing the optimization method: a surface-forced tracer (SFT) and an entrainment-forced tracer (EFT) (Wyngaard and Brost 1984; Chor et al. 2020b). An SFT is one that has a source at the surface and no other sources/sinks inside the domain. Figure 1a shows the normalized mean turbulent flux profile for an SFT from a convective regime, which will be detailed in section 3. SFTs are known to be effectively transported by large convective plumes (Kaimal et al. 1976; Wyngaard and Brost 1984; Moeng and Sullivan 1994), which is sketched in Fig. 1a as red arrows. In the case of wavy oceanic regimes SFTs are also thought to be efficiently transported vertically by Langmuir circulations.

An EFT, on the other hand, is defined as a tracer whose flux into the mixed layer is performed solely by entrainment

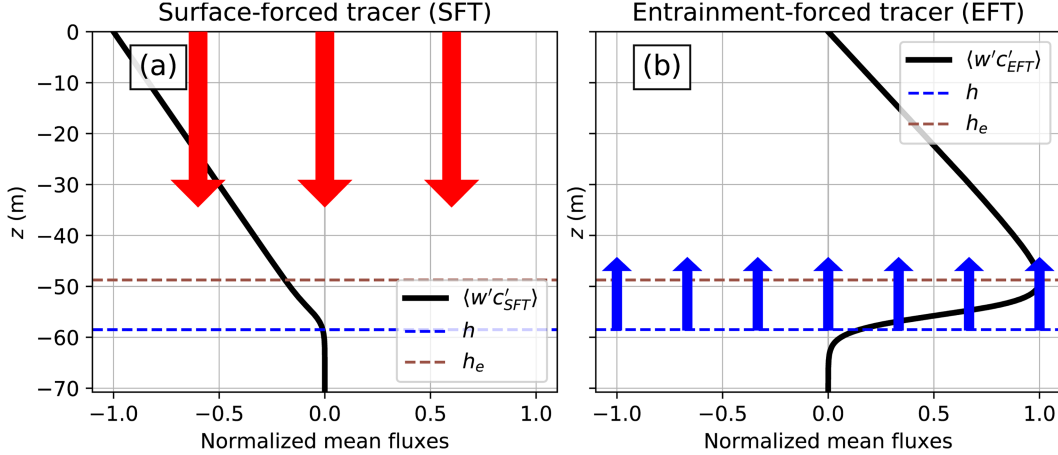


FIG. 1. Mean turbulent flux profiles for (a) an SFT and (b) an EFT. The data for this plot are taken from a convective simulation without surface wind shear or waves, to be described in section 3. Both fluxes are normalized so that the maximum magnitude of the fluxes is unity. Sketched in the figure are also arrows for transport via coherent convective plumes (red arrows) and entrainment processes (blue arrows), along with the boundary layer depth h .

processes. Vertical transport of this tracer is not as efficient as that of SFTs since there are no large coherent structures emerging from the entrainment layer. Figure 1b shows the mean turbulent flux profile for an EFT as a solid black line from the same convective simulation used in Fig. 1a. In practice this flux occurs due to a change in concentration across the entrainment layer, and its mechanism is sketched in Fig. 1b as blue arrows. It should be noted that, since the transport equations are linear for passive tracers, tracers that are linear combinations of SFTs and EFTs are also solutions of the flow. We also use EFTs to define the maximum entrainment depth h_e , which is the depth at which the turbulent flux of an EFT is at its maximum (depicted as a dashed brown line in Fig. 1).

While there are many ways to define the boundary layer depth h , it is generally understood that it should represent the maximum depth that OSBL eddies can penetrate into the stratified fluid (Li et al. 2016). In the absence of other sources of instabilities (as is the case with our simulations, described in section 3), OSBL eddies emerge from surface processes. Thus, we define h as the depth at which the SFT turbulent flux $\langle w'c'_{SFT} \rangle$ reaches roughly zero—in our convention h is a negative number. We prefer this definition because it matches very closely to the maximum buoyancy gradient criterion used in Li and Fox-Kemper (2017) for convective conditions, which has its relations to other estimates mapped out (see Fig. 1b of Li and Fox-Kemper 2017). The boundary layer depth h can be seen in Fig. 1 as a dashed blue line. From here on we prioritize using the normalized vertical coordinate $\sigma = z/h > 0$ for depth, instead of using z .

We define the turbulent Langmuir number as

$$\text{La}_t = (u_*/u_0^s)^{1/2}, \quad (2)$$

where $u_* = \sqrt{\langle u'w' \rangle_s}$ is the friction velocity ($\langle u'w' \rangle_s$ is the average momentum flux at the surface) and u_0^s is the Stokes drift at the surface (McWilliams et al. 1997). The La_t assumes that

most information on nonbreaking waves can be obtained by u_0^s . However, this ignores other aspects of the Stokes drift such as its penetration and at times may not be sufficient for the characterization of nonbreaking waves (Li et al. 2019). For that reason, Harcourt and D'Asaro (2008) introduced the surface-layer Langmuir number La_{SL} , defined as

$$\text{La}_{\text{SL}} = \left(\frac{u_*}{\langle u^s \rangle - u_{\text{ref}}^s} \right)^{1/2}, \quad (3)$$

where $\langle u^s \rangle$ is a surface-layer-averaged Stokes drift (in this case $0 \leq \sigma \leq 0.2$) and u_{ref}^s is a reference Stokes drift (taken at $\sigma = 0.765$). A few definitions exist that generalize this parameter to the case in which wind and waves are misaligned (Van Roekel et al. 2012; Reichl et al. 2016) and that tend to exclude u_{ref}^s in the denominator. Since we only investigate regimes with wind-aligned waves and since u_{ref}^s is too small in our simulations to make any significant impact, we use Eq. (3) to calculate La_{SL} for all simulations in this work.

We also define the stability parameter Λ as

$$\Lambda = \kappa w_*^3/u_*^3, \quad (4)$$

where κ is the von Kármán constant, $w_* = (B_s|h|)^{1/3}$ is the turbulent convective velocity (Kaimal et al. 1976). Here B_s is the surface buoyancy flux and positive values imply a loss of buoyancy. Λ is equivalent to $-|h|/L_o$, where L_o is the Obukhov length, with negative values of Λ indicating stable conditions and positive values indicating unstable conditions. Last, we define a Langmuir velocity scale as $w_L = (u_*^2 u_0^s)^{1/3}$ (Harcourt and D'Asaro 2008).

It is useful to assume that u_0^s is sufficient to characterize the effects of waves (which may be of limited realism) since in that case La_t and Λ are sufficient to characterize any oceanic regime with only waves, surface wind stress and surface buoyancy fluxes as forcings. Based on this assumption we use a modified

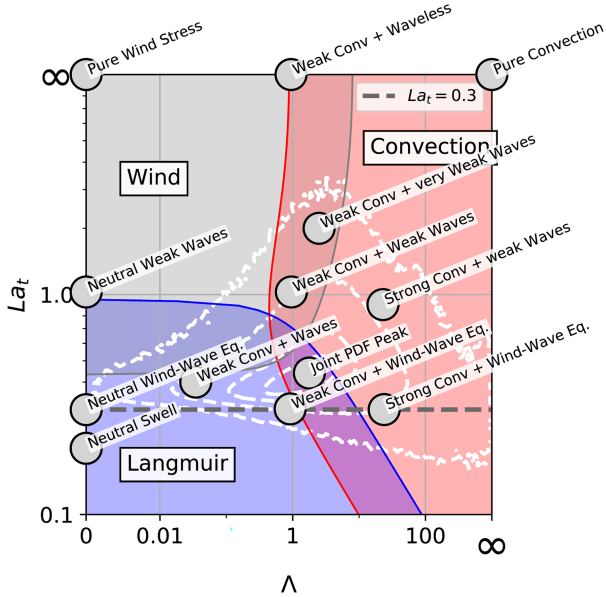


FIG. 2. All simulations used in this paper, shown as gray circles in an La_t - Λ parameter space. Solid blue, gray, and red lines delineate regions where at least 25% of the turbulent kinetic energy is produced by Langmuir (blue), surface wind stress (gray), and buoyancy fluxes (pink), respectively. Intersection areas are dominated by more than one forcing. Dashed white lines are the joint PDF of oceanic regimes from Li et al. (2019), and the dashed gray line marks the line of wind-wave equilibrium. Note that most of the figure is in logarithmic scale except the range $0 \leq \Lambda \leq 1 \times 10^{-2}$ and that the top and right edges represent infinity. Note also that a Pure Convection simulation (where $\Lambda \rightarrow \infty$ and La_t is not defined since $u_* = u_0^s = 0$) is plotted as if $\text{La}_t = \infty$.

version of the regime diagram (seen in Fig. 2) introduced by Li et al. (2005) and Belcher et al. (2012) in which the axes are La_t and Λ (we constrain ourselves to unstable regimes, designated by $\Lambda \geq 0$). In most versions of the diagram, convection was measured with $w_*^3/w_L^3 = \text{La}_t^2 \Lambda / \kappa$ [an exception being Fig. 9 of Li and Fox-Kemper (2017), which uses Λ/κ], which contains an implicit dependence on the Langmuir number that we try to avoid. Furthermore, Λ is common in the atmospheric literature, making the transfer of knowledge between both fields more straightforward. Each of the three regions of the diagram delineates an area where one of the three forcings dominates, while overlapping areas are dominated by more than one forcing. We also plot the joint probability density function (joint PDF) for ocean regimes taken from the set of simulations in Li et al. (2019) as dashed white lines as a guide to assess representativeness of regimes.

b. Current KPP formulation

Several versions of KPP have been proposed, most of which with different formulations to include wave effects. A thorough review is outside the scope of this paper, and the reader is directed to Li et al. (2019) for details. The focus of this paper is on the formulation of $K(\sigma)$ and $F_{\text{ND}}(\sigma)$, and we leave other aspects of KPP (e.g., the estimation of the OSBL depth)

untouched. Most formulations of KPP that include wave effects can be written generally for unstable conditions as

$$K(\sigma) = u_s(\sigma) |h| G_k(\sigma), \quad (5)$$

$$u_s(\sigma) = \mathcal{E}(\text{La}_t) \frac{\kappa u_*}{\phi(z/L_o)}, \quad \text{and} \quad (6)$$

$$F_{\text{ND}}(\sigma) = G_s(\sigma) \langle w' c' \rangle_s, \quad (7)$$

which we will also adopt in this paper except for the addition of a few extra dependencies. Here $\kappa = 0.4$ is the von Kármán constant, $\phi(z/L_o)$ is the nondimensional gradient for a tracer in the surface layer according to MOST, $G_k(\sigma)$ is a nondimensional shape function for $K(\sigma)$ and $G_s(\sigma)$ is a nondimensional shape function for the surface-driven nondiffusive flux. The velocity scale u_s is capped at its value at $\sigma = 0.1$ for unstable conditions according to most implementations (Large et al. 1994). Parameter \mathcal{E} is a Langmuir enhancement parameter that depends at least on the Langmuir number La_t , but may depend on other variables (Smyth et al. 2002; Reichl et al. 2016). For example, in the face of the results in section 4 and previous studies, we may expect $\mathcal{E}(\text{La}_t, \Lambda)$ in some cases (Smyth et al. 2002; Li and Fox-Kemper 2017).

In most previous versions of KPP, the eddy diffusivity $K(\sigma)$ and the nondiffusive fluxes $F_{\text{ND}}(\sigma)$ were limited to having the same shape. That is, $G_k = G_s/C_s = G_n$, where $C_s = 5\kappa(0.1c_s\kappa)^{1/3}$ is a nondimensional constant [c_s is another nondimensional constant that depends on the chosen formulation for $\phi(z/L_o)$, which we take from Large et al. (1994) to be $c_s = 98.96$] and $G_n(\sigma)$ is a cubic function that originated in the neutral atmospheric boundary layer literature:

$$G_n(\sigma) = \sigma(1 - \sigma)^2. \quad (8)$$

The reasons for a cubic shape are (i) that it is the lowest degree polynomial that can satisfy all four physically motivated boundary conditions for $K(\sigma)$ (O'Brien 1970) and (ii) that a cubic shape matches the estimated $K(\sigma)$ profile for a neutral and waveless simulation (Large et al. 1994; Marlatt et al. 2012).

Although there are a few exceptions that may not fit Eqs. (5)–(8) (e.g., Yang et al. 2015; Sinha et al. 2015; Large et al. 2019b), these equations indicate that in most cases the only adjustment in the KPP profiles for wavy conditions is a change in the magnitude of the eddy diffusivity $K(\sigma)$ that is accomplished by \mathcal{E} . As such, most of the difference between different KPP versions is generally confined to formulation used for \mathcal{E} [vide Fig. A1 of Li et al. (2019) for a visual comparison].

In particular, most previous models include no changes in the shape of $K(\sigma)$, which is given by the cubic profile $G_n(\sigma)$ in every regime, or the shape and magnitude of $G_s(\sigma)$, despite evidence indicating that Langmuir circulations affect non-diffusive vertical transport (Chen et al. 2016). Due to the limiting nature of these assumptions and the lack of evidence to support their necessity we relax them here, allowing $G_k(\sigma)$ and $G_s(\sigma)$ to be different from each other and from $G_n(\sigma)$. Furthermore we allow $G_s(\sigma)$ to also depend on Λ and La_t , for reasons that will become clearer in section 4.

Note that Large et al. (2019a) recently introduced a modified version of MOST for the ocean that includes alternative formulations for $u_s(\sigma)$ for waveless regimes (different from the ones used for the atmosphere) and new formulations for wavy ones. However, we choose to not use their theory here since we believe that more data are needed in order to validate those results.

c. A new flux partition model

We base the analyses of this and the following section on the framework developed in Chor et al. (2020b). Sufficient information to follow the reasoning is given but the reader is directed to the original paper for more details. We consider a three-term flux decomposition without imposing any shape or scaling for $K(\sigma)$ and apply it to an SFT and an EFT as

$$\begin{aligned} \langle w'c'_{\text{SFT}} \rangle &= -K(\sigma) \frac{\partial \langle C_{\text{SFT}} \rangle}{\partial \sigma} + \langle w'c'_{\text{SFT}} \rangle_e G_e(\sigma) \\ &\quad + \langle w'c'_{\text{SFT}} \rangle_s G_s(\sigma) \quad \text{and} \end{aligned} \quad (9)$$

$$\langle w'c'_{\text{EFT}} \rangle = -K(\sigma) \frac{\partial \langle C_{\text{EFT}} \rangle}{\partial \sigma} + \langle w'c'_{\text{EFT}} \rangle_e G_e(\sigma). \quad (10)$$

where the subscripts identify an SFT or EFT quantity, $\langle w'c' \rangle_s$ and $\langle w'c' \rangle_e$ are the values of the turbulent flux taken at the surface and at h_e , respectively. Furthermore, $G_s(\sigma)$ and $G_e(\sigma)$ are (as of now) unspecified dimensionless shape functions associated with surface and entrainment processes, respectively.

$K(\sigma)$, $G_s(\sigma)$, and $G_e(\sigma)$ are assumed to be functions of the flow alone, and knowledge of those three profiles is sufficient to reconstruct the total flux of any passive tracer provided that the fluxes at the vertical boundaries of the OSBL are known. Given our focus on diagnostic analyses, we obtain $\langle w'c' \rangle_s$ and $\langle w'c' \rangle_e$ from large-eddy simulations (LES) results. Note that while an SFT has both components of the nondiffusive flux (since there may be a small flux of C_{SFT} through h_e), an EFT only has the entrainment-driven flux, since $\langle w'c'_{\text{EFT}} \rangle_s = 0$ as a boundary condition.

The main difference between our flux separation and previous approaches is that we separate the nondiffusive flux F_{ND} into two components (due to surface and entrainment processes separately), while previous approaches only consider one component. While we show in section 4 that $G_e(\sigma)$ is likely not important in modeling applications (since its magnitude is small in all cases considered here), it is critical when applying our method (see appendix of Chor et al. 2020b).

$K(\sigma)$, $G_s(\sigma)$, and $G_e(\sigma)$ need to be estimated, which introduces the need for an extra equation in addition to Eqs. (9) and (10). We follow Chor et al. (2020b) and use an optimization method that uses only fluxes and mean scalar gradients of SFTs and EFTs in order to close the system of equations. To that end, we introduce a cost function χ to be minimized in an optimization procedure:

$$\chi = G_s(\sigma)^2 + G_e(\sigma)^2. \quad (11)$$

This choice of χ is designed to minimize nondiffusive fluxes F_{ND} , which ensures that the flux is fully diffusive in regimes where most of the eddies tend to be small (e.g., in waveless stable or neutral conditions; Jayaraman and Brasseur 2018).

Furthermore, diffusive operators are known to work in a variety of conditions (Corrsin 1975), are numerically well behaved (since they always decrease integrated variance of the transported scalar) and they avoid some issues that exist with non-diffusive fluxes (see section 8.6.4 of Griffies et al. 2015). Thus, trying to model as much of the flux as possible with a diffusive operator is also a modeling-motivated decision.

We emphasize that, although it is common practice to conceptually think of the diffusive/nondiffusive flux decomposition as a physical one, that separation is artificial. The need for a nondiffusive component comes from having large coherent structures in the flow (Deardorff 1966), but there does not need to be one-to-one correspondence between nondiffusive fluxes and large eddies. In fact there is evidence that the flux due to large structures in convective flows is different from the nondiffusive flux of KPP (Zhou et al. 2018). As such, even though χ is partially physically motivated, our method should not be seen as providing a completely physical partition of the fluxes (because a physical decomposition of turbulent fluxes into diffusive and nondiffusive components is impossible). Thus, care should be taken when trying to interpret our results (or any other KPP-like decomposition results) in a completely physical framework.

With that said, by maximizing the eddy diffusivity we ensure that only the asymmetric part of the vertical transport is allocated to the nondiffusive component. So in essence, due to our definition of χ , the nondiffusive flux can be seen as a measure of the asymmetry in the vertical transport in the OSBL.

As an explanatory example, consider a neutral waveless regime, where there is almost no asymmetry in the vertical transport (i.e., transport from surface down is as efficient as transport from the entrainment up). In this case all the transport can be represented using a diffusive term and there is no need for a nondiffusive component. Langmuir turbulence and convection change this flow in two main ways: (i) they enhance mixing and transport efficiency and (ii) they introduce vertical transport asymmetry, since now the transport from the surface down is more efficient than the transport from the entrainment up. The enhancement i can be modeled as diffusive behavior even though it may be caused by large-scale coherent motions. However, the transport asymmetry ii needs to be accounted for by a nondiffusive term otherwise the resulting eddy diffusivity may become negative or even singular (Wyngaard and Brost 1984). Thus, by minimizing nondiffusive fluxes, we ensure that they are used only in the cases where vertical transport asymmetry makes it necessary, which generally coincides with regimes that have a prevalence of large coherent structures.

The constraint $K \geq 0$ is enforced in the optimization but G_e and G_s are left unconstrained and can become negative. Allowing negative values of the shape functions can potentially impact KPP in two ways. (i) It may exacerbate an known unphysical behavior where a tracer source at the surface leads to a reduction of tracer mass in portions of the OSBL directly due to the nondiffusive component (which is generally discussed in terms of temperature and therefore cooling/heating). (ii) Moreover, regions with a negative value of G_s imply that the nondiffusive flux is in the opposite sign of the surface flux itself (and similarly for G_e and the entrainment flux).

TABLE 2. Parameters for the simulations used in this paper. All simulations have 256 points in the horizontal direction and 400 points in the vertical direction, with 400-m horizontal domain and 150-m vertical domain. Note that in simulation Pure Convection the actual Langmuir number is undefined since $u_* = u_0^* = 0$, but we report it as $La_t \rightarrow \infty$ since this limit represents waveless conditions and because it makes it possible to plot it in the La_t - Λ parameter space.

Simulation	u_* (ms^{-1})	B_s ($\text{m}^2 \text{s}^{-3}$)	Λ	La_t	h_e (m)	h (m)
Neutral Swell	6.1×10^{-3}	0.00	0.00	0.20	-55.9	-66.8
Neutral Wind-Wave Eq.	6.1×10^{-3}	0.00	0.00	0.30	-57.0	-67.5
Neutral Weak Waves	7.0×10^{-3}	0.00	0.00	1.03	-49.9	-60.0
Pure Wind Stress	1.0×10^{-2}	0.00	0.00	∞	-50.2	-60.0
Weak Conv + Waves	6.1×10^{-3}	2.92×10^{-10}	3.46×10^{-2}	0.40	-55.1	-66.8
Weak Conv + Wind-Wave Eq.	7.0×10^{-3}	1.27×10^{-8}	9.17×10^{-1}	0.30	-52.5	-61.9
Weak Conv + Waveless	7.0×10^{-3}	1.27×10^{-8}	9.44×10^{-1}	∞	-54.4	-63.8
Weak Conv + Weak Waves	7.0×10^{-3}	1.27×10^{-8}	9.56×10^{-1}	1.03	-54.8	-64.5
Joint PDF Peak	7.0×10^{-3}	2.35×10^{-8}	1.78	0.44	-54.8	-64.9
Weak Conv + very Weak Waves	7.0×10^{-3}	3.14×10^{-8}	2.50	2.00	-56.2	-68.2
Strong Conv + weak Waves	4.0×10^{-3}	5.90×10^{-8}	2.29×10^1	0.90	-52.9	-62.2
Strong Conv + Wind-Wave Eq.	4.0×10^{-3}	5.90×10^{-8}	2.39×10^1	0.30	-55.1	-64.9
Pure Convection	0.0	9.23×10^{-8}	∞	—	-48.8	-58.5

We note that i happens for any convex shape function, which implies that $dG_s/d\sigma$ changes sign in the domain [see discussion in section 8.6.4 of Griffies et al. (2015)] regardless of it having negative values. Furthermore, i and ii are only an issue in the absence of diffusive fluxes, which should be a rare occasion under normal conditions. In fact, since our method minimizes nondiffusive fluxes, it is possible that it alleviates these issues by simply increasing the prevalence of diffusive fluxes. Last, while we allow negative values of G_s and G_e , G_e tends to be small in magnitude and is not used in the considered modifications for KPP. Moreover, occasions where $G_s < 0$ happen very rarely in our results and do not change the analyses significantly. This will become clear when proposing a different formulation for $G_s(\sigma)$ based on diagnosed shape functions in section 6, where the new shape (shown in Fig. 6c) can be seen to have nonnegative values throughout the domain.

3. Numerical aspects

We use an LES model that was already used successfully in other studies (Yang et al. 2015; Chor et al. 2018) to apply the methods described in section 2. The model solves the Craik-Leibovich equations (Craik and Leibovich 1976) and employs a pseudospectral scheme in the horizontal directions and a centered finite differences in the vertical direction to solve the flow. The tracer advection is solved using a finite volume scheme with bounded advection (Chamecki et al. 2008). Horizontal boundary conditions are doubly periodic and the subgrid-scale model used is the Lagrangian-averaged scale-dependent model (Bou-Zeid et al. 2005), which has been shown to reach statistical convergence at coarser resolutions than different subgrid-scale closures (Salesky et al. 2017).

We run 13 simulations in total, which are plotted in the La_t - Λ parameter space in Fig. 2 as gray circles and have their characteristics listed in Table 2. Although there are no simulations in the areas dominated by both wind stress and Langmuir, or dominated by all three forcings simultaneously, we do not

consider this to be a problem since the limits of these areas are approximate. Note that for the Pure Convection simulation, La_t is undefined since $u_* = u_0^* = 0$, but we report it as $La_t \rightarrow \infty$ for ease of analysis since this limit represents simulations without waves.

In all cases the rotation frequency is $f_0 = 7 \times 10^{-5} \text{ s}^{-1}$, the domain is $400 \times 400 \times 150$ meters and the grid has 256 points in the horizontal directions and 400 in the vertical direction. The initial potential temperature (θ) profile is well mixed until approximately 0.85 h with a constant gradient of $2 \times 10^{-2} \text{ km}^{-1}$ below it. For ease of the reader, each simulations has a specific name (that can be found in Table 2) that gives an approximated brief description of that simulation.

Wave effects were introduced by imposing a Stokes drift profile in each simulation. All simulations that have wave effects are listed in Table 3 along with their respective wave characteristics, otherwise the imposed Stokes profile is identically zero. For the sake of control over La_t and the Stokes profile in general, all waves in this paper are monochromatic and thus can be fully defined by setting a wavelength L_w and a wave amplitude a (McWilliams et al. 1997). Using monochromatic waves also avoids vertical resolution issues from having to resolve the superexponential decay of broadband wave spectra near the surface.

We minimized the effects of inertial oscillations by setting the initial conditions for velocity to their average over one inertial period (taken from identical simulations on a coarser grid that were run over many inertial periods specifically for this purpose). We verified that after this procedure inertial effects were not visible in averaged results regardless of the averaging period. All of the simulations had a spinup period of at least eight eddy turnover times T_* , and the statistics were collected during the next $6.5T_*$ period or longer. Eddy turnover times are calculated as $T_* = |h| \max(u_*, w_*, w_L)$.

All simulations also have an SFT and an EFT (both passively transported by the flow) with concentrations C_{SFT} and C_{EFT} that have different initial and boundary conditions. Entrainment fluxes are accomplished by imposing different

TABLE 3. Wave parameters for simulations used in this paper that include wave effects. For all other simulations the Stokes drift is identically zero. Here, D_{st} is the e -folding depth of the Stokes profile, given by $D_{st} = L_w/(4\pi)$ for monochromatic wave spectra.

Simulation	a (m)	L_w (m)	La_{SL}	u_0^s (ms^{-1})	D_{st} (m)
Neutral Swell	2.00	120.0	0.28	1.5×10^{-1}	9.5
Neutral Wind-Wave Eq.	0.80	60.0	0.52	6.8×10^{-2}	4.8
Neutral Weak Waves	0.25	60.0	1.70	6.6×10^{-3}	4.8
Weak Conv + Waves	0.60	60.0	0.69	3.8×10^{-2}	4.8
Weak Conv + Wind-Wave Eq.	0.85	60.0	0.51	7.7×10^{-2}	4.8
Weak Conv + Weak Waves	0.25	60.0	1.74	6.6×10^{-3}	4.8
Joint PDF Peak	0.58	60.0	0.75	3.6×10^{-2}	4.8
Weak Conv + very Weak Waves	0.13	60.0	3.47	1.7×10^{-3}	4.8
Strong Conv + weak Waves	0.22	60.0	1.51	4.9×10^{-3}	4.8
Strong Conv + Wind-Wave Eq.	0.65	60.0	0.51	4.5×10^{-2}	4.8

initial concentrations for the mixed layer and below it. Thus, EFTs are initialized with zero concentration until approximately $0.9h$ and nonzero concentration below. SFTs are initialized with a $C_{SFT} = 0$ throughout the domain. EFTs have a zero-flux boundary condition at the surface, while we impose a nonzero surface mass flux into the OSBL for SFTs. Both tracers have horizontally periodic boundary conditions. Throughout this paper all tracer fluxes are normalized either by their value at the surface (for SFTs) or by their entrainment fluxes (for EFTs).

4. Results

After the method is applied and profiles for $K(\sigma)$, $G_s(\sigma)$, and $G_e(\sigma)$ are obtained, F_D and F_{ND} can be calculated. In this section we present the results for F_D and F_{ND} based on our decomposition, and then move on to discuss the eddy diffusivity and shape function profiles in more detail.

a. Flux decompositions

Figure 3 shows the turbulent flux decomposition for Simulation Neutral Wind-Wave Eq., which is similar to the main simulation in McWilliams et al. (1997) but with $\Lambda = 0$. Figure 3a shows results for an SFT and it is evident that SFT nondiffusive fluxes are significant in this regime, accounting for around 40% of the total turbulent flux in the middle of the OSBL (see Fig. 3c, which shows the metric $|F_{ND}|/(|F_{ND}| + |F_D|)$, which simplifies to the ratio of nondiffusive to total fluxes whenever F_{ND} and F_D are both positive). Although not shown for brevity, it is important to mention that our optimization method correctly captures the physical behavior in regimes known to not need nondiffusive fluxes [e.g., the Pure Wind Stress simulation, shown in the online supplemental material, and the neutral simulation of Chor et al. (2020b) are diagnosed by our method to have negligible nondiffusive fluxes]. With that in mind, since there is no convection in this regime, the nondiffusive term visible in Fig. 3a must be the product of Langmuir circulations. Since the calculation of these fluxes assumes a minimization of the nondiffusive fluxes (see discussion in section 2c), this is evidence that nondiffusive fluxes *must* be present when modeling regimes with nonbreaking waves. Furthermore, SFT fluxes in the surface layer are fully diffusive, as expected from MOST. EFTs have very little nondiffusive

fluxes in this regime, indicating a lower importance of non-diffusive entrainment processes.

Throughout all simulations in this work (shown in the online supplemental material), repeated patterns are (i) fully diffusive fluxes in the surface and entrainment layers for SFTs independent of the regime; (ii) significant nondiffusive SFT fluxes in the middle of the OSBL whenever large eddies are present (either due to convection or nonbreaking waves) with a peak close to the middle of the OSBL; and (iii) little contribution from non-diffusive fluxes for EFTs. Whenever present, the shapes of non-diffusive fluxes are also similar to those in Fig. 3. Thus, in order to avoid analyzing all simulations with this level of detail, we take a bulk approach and define

$$R_F = \frac{\int_0^1 |F_{ND}| d\sigma}{\int_0^1 (|F_D| + |F_{ND}|) d\sigma}, \quad (12)$$

which indicates the importance of nondiffusive fluxes relative to total turbulent fluxes. R_F is bounded between 0 (fully diffusive) and 1 (fully nondiffusive). Because of the possibility of flux components having opposite signs, interpreting R_F as a percentage of fluxes is not precisely correct. However, as this happens very rarely for SFTs and for small percentage of the OSBL for EFTs, this is a valid approximation. Recall also that, given our definition of the cost function χ and its implication for the diagnosed nondiffusive fluxes, R_F can also be interpreted as a bulk measure of the vertical transport asymmetry of the flow. In this case $R_F = 0$ would indicate a flow with perfect vertical transport symmetry (transport from the surface down being as efficient as transport from the entrainment up), and contrarily for $R_F = 1$.

Results for R_F are shown in Fig. 4a for SFTs and Fig. 4b for EFTs. It becomes immediately clear that R_F values for EFT are much lower than SFTs throughout the parameter space, with the Pure Wind Stress case being the only exception. The magnitude of R_F for EFTs suggests that entrainment-driven nondiffusive transport is always smaller than 10% of the total flux (the maximum value of R_F for EFTs is 0.09). Note that the percentage of nondiffusive to total EFT fluxes can be higher at specific depths for some regimes.

The R_F values for SFTs, however, indicate that surface-driven nondiffusive transport can account for approximately

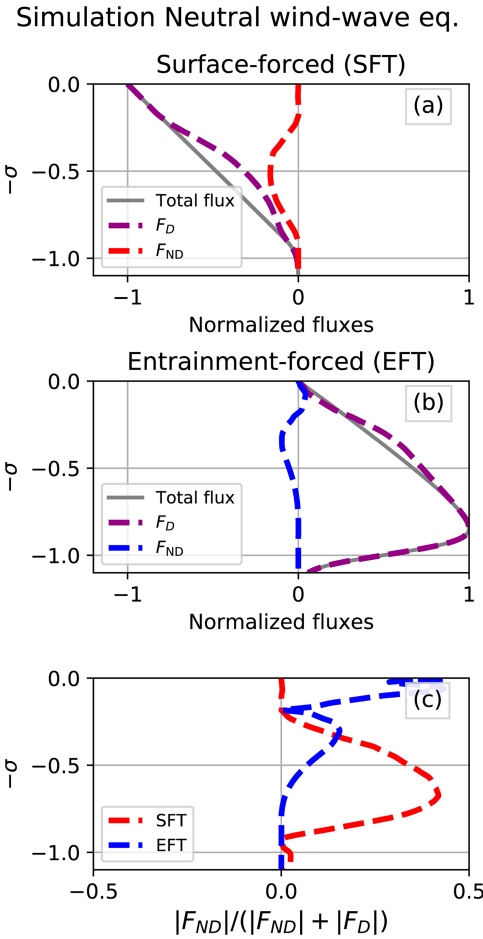


FIG. 3. Flux decomposition for Simulation Neutral Wind-Wave Eq. showing the decomposition for (a) an SFT and (b) an EFT. (c) The metric $|F_{ND}|/(|F_{ND}| + |F_D|)$. The absolute value operators are used to account for the cancellations that occur for the EFT.

50% of the total flux (the maximum value is 48% for simulation Weak Conv + Very Weak Waves). In fact, every simulation that is not the Pure Wind Stress simulation ($\text{La}_t \rightarrow \infty$, $\Lambda = 0$) has more than 10% of nondiffusive fluxes. The fact that nondiffusive fluxes are important even when minimizing them points to their indispensability in KPP-like models. In particular, we see a significant presence of nondiffusive fluxes for neutral simulations with waves (corresponding to the line $\Lambda = 0$ on the left edge of the parameter space). As an example, F_{ND} accounts for 15% of the total flux in Simulation Neutral Wind-Wave Eq. This value is not as large as R_F for the Pure Convection simulations (approximately 35%), but it is significant. Since our method minimizes F_{ND} , this is the lower bound for nondiffusive fluxes, which points to the need of considering waves in the formulation of F_{ND} .

Furthermore, it is interesting to see that the peak values of R_F for SFTs happen when there are weak waves and moderate convection, which has higher values of R_F than the Pure Convection simulation. This points to some interaction between Langmuir circulations and convective plumes, even though the

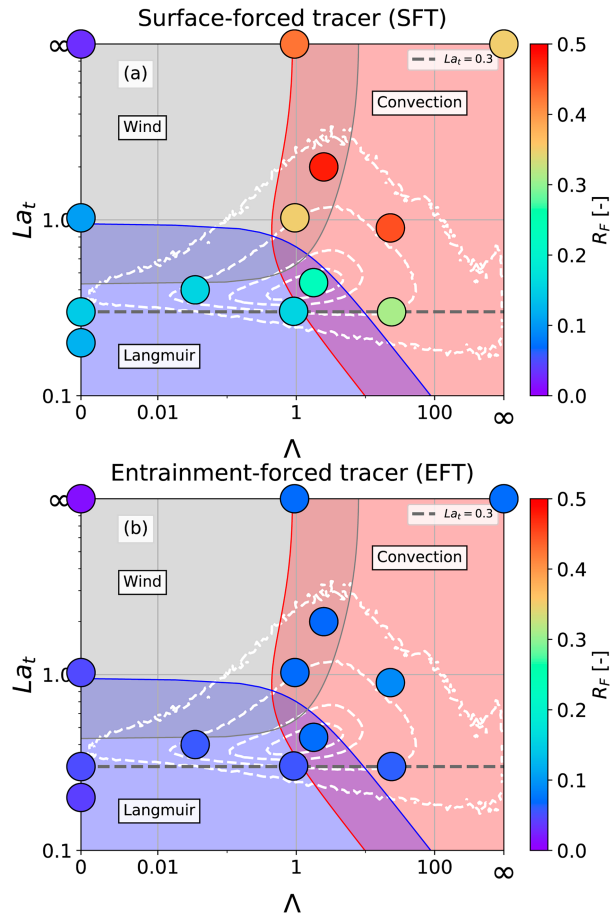


FIG. 4. Ratio of nondiffusive to total fluxes R_F [defined in Eq. (12)] for each individual simulation plotted on top of the La_t - Λ parameter space as colored circles. Shown are (a) the results for SFTs and (b) the results for EFTs.

flux decomposition profiles show no qualitative difference from the other regimes (see the online supplemental material).

b. Eddy diffusivity shapes

Figure 5 shows $K(\sigma)$ for selected simulations obtained with our optimization method (black) along with estimates from different models in the literature for comparison (colored lines). The cases that are not shown follow similar patterns. It is clear that model predictions differ from our optimized results for both magnitude and shape of $K(\sigma)$ in most cases.

Considering the profiles shown in Fig. 5 and the rest of our results (in the online supplemental material) we see that the optimized eddy diffusivity shapes are very similar to each other whenever waves are present. This can be seen in Fig. 6a where we show $K(\sigma)$ normalized by its integral over σ (in order to focus on the shapes as opposed to the magnitudes) for all regimes with waves (solid black lines). It is clear that all shapes in wavy regimes are similar to each other, and that they are different from the community-standard cubic function $G_n(\sigma)$ (dashed gray line). The same quantities for regimes without waves are plotted in Fig. 6b for reference, where a clear

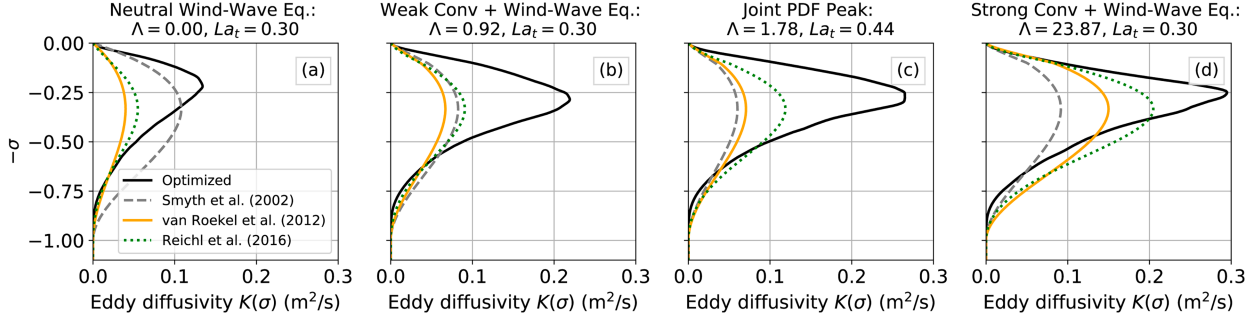


FIG. 5. Eddy diffusivity profiles $K(\sigma)$ for some of the simulations in this paper. Black lines are results from our optimization method, gray lines show results from the model by [Smyth et al. \(2002\)](#), orange lines represent the model by [Van Roeke et al. \(2012\)](#) with aligned wind and waves, and green lines represent the model by [Reichl et al. \(2016\)](#).

mismatch between them is evident. We also plot the average eddy diffusivity shape for wavy regimes $\mathcal{G}_l(\sigma)$ (green dashed line in Fig. 6a), which will be used later in the paper to modify the traditional KPP.

Results in Figs. 6a and 6b indicate that the presence of waves changes the eddy diffusivity shapes in a way that does not depend on either the precise characteristics of the waves or the strength of the convection. This rough collapse into one specific shape [$\mathcal{G}_l(\sigma)$] makes it possible to seek a universal fixed curve for KPP in wavy situations that should be different from the cubic shape. This is further explored in section 6.

c. Nondiffusive flux shapes $G_s(\sigma)$

Results for the surface-driven nondiffusive shape functions $G_s(\sigma)$ are shown in Fig. 7, where the line colors follow those

of Fig. 5. Our results indicate that the nondimensional shape profile for nondiffusive surface transport $G_s(\sigma)$ can change between regimes, dependent on the surface flux, which is something previous KPP versions do not consider. This suggests that $G_s(\sigma)$ should depend on the magnitude of surface buoyancy fluxes, and not just their presence (as is the case with current formulations). Figure 7a also indicates that the effect of Langmuir circulations on $G_s(\sigma)$ is also significant [given that it is a neutral simulation with waves and nonzero $G_s(\sigma)$], which is a conclusion that follows directly from the flux partition shown in Fig. 3.

Furthermore, it appears that the shapes of $G_s(\sigma)$ obtained from our method for wavy regimes are also different from the commonly used cubic shape in KPP-like models. To better explore that, we also plot $G_s(\sigma)$ for the wavy cases in Fig. 6c.

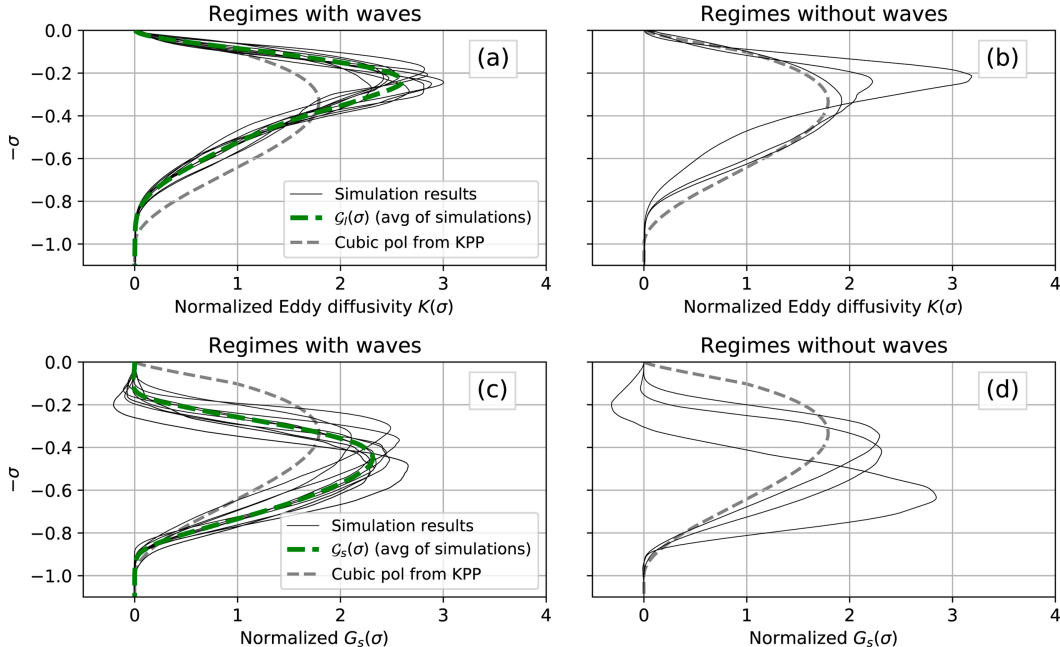


FIG. 6. (a),(b) Eddy diffusivity and (c),(d) nondiffusive surface flux shapes normalized by their integral over σ for (left) results from wavy regimes only and (right) results from waveless regimes only. Black lines are results from all regimes in this paper using our optimization method. Dashed gray lines are the cubic shape function $G_n(\sigma)$ for reference, and dashed green lines represent the empirical curve, which is the average of the wavy simulations.

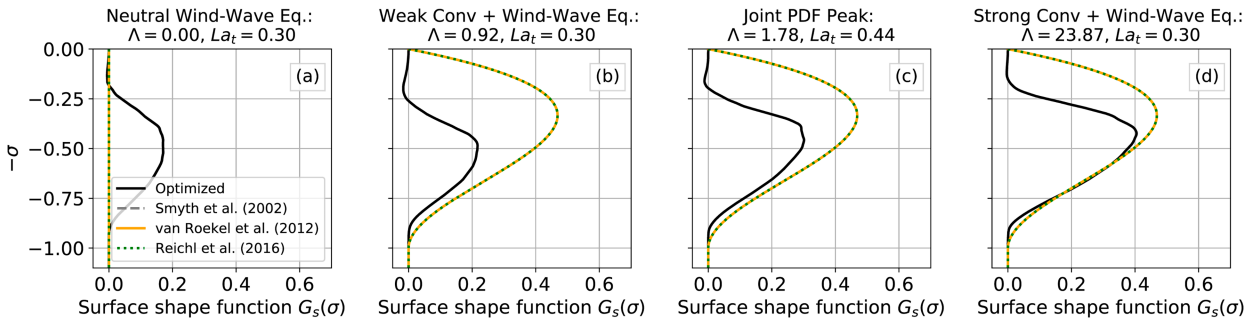


FIG. 7. Nondiffusive surface shape functions $G_s(\sigma)$ for selected simulations (same simulations as in Fig. 5). Black lines show results from our optimization method, and colored lines represent results from literature models where $G_s(\sigma) = \mathcal{C}_s G_n(\sigma)$ (Smyth et al. 2002; Van Roekel et al. 2012; Reichl et al. 2016). Note that all colored lines coincide either because the authors explicitly use the same formulation [the case for Large et al. (1994) and Smyth et al. (2002)] or because the authors did not explore convective conditions, and (for the purposes of this work) we complete KPP in these cases with the default shape from Large et al. (1994) for the nondiffusive component [the case for Van Roekel et al. (2012) and Reichl et al. (2016)].

where results are again normalized by their integral over σ in order to focus on shapes. There is clearly significant difference between the traditional KPP model profile (dashed gray line) and our optimization results (solid black lines), especially close to the surface. While the cubic profile produces significant amount of nondiffusive fluxes in the surface layer, profiles from our method are approximately zero in that region, which is in accordance with MOST. Furthermore, the similarity of profiles in wavy regimes once again suggests that the presence of waves collapses profile shapes, creating a somewhat wave-universal shape $\mathcal{G}_s(\sigma)$ that does not depend on other characteristics of the flow. $\mathcal{G}_s(\sigma)$, which is the average of the solid black lines for wavy regimes, is shown as a dashed green line in Fig. 6c. We also show $G_s(\sigma)$ for waveless regimes in Fig. 6d for reference, where the mismatch between simulations is clear.

d. Enhancement factors \mathcal{E}

It is useful to separate our eddy diffusivities in a shape and a scaling, according to previous models. We focus for now on wavy regimes and use the average of eddy diffusivity shapes $\mathcal{G}_l(\sigma)$ (shown as a green line in Fig. 6a) to define

$$G_l(\sigma) = \frac{1}{A^*} \mathcal{G}_l(\sigma) \quad (13)$$

where A^* is a constant that is used solely to impose that $dG_l(\sigma)/d\sigma = 1$ at the surface. Thus $A^* = d\mathcal{G}_l(\sigma)/d\sigma$ at $\sigma = 0$. More information about this shape and instructions for implementation are given in the appendix.

Since $G_l(\sigma)$ only contains information from regimes with waves, it is an empirical shape function appropriate for wavy (or Langmuir) regimes at expense of some accuracy for waveless ones. Since waveless regimes are uncommon in the ocean we believe this to be a well-founded choice, with the possible caveat of ice-covered regions. Nonetheless, in order to retain compliance with the canonical case of neutral waveless oceans (wind stress-dominated regime) in the analyses to follow, we postulate an alternative formulation for $G_k(\sigma)$ as

$$G_k(\sigma) = \begin{cases} G_n(\sigma) & \text{if } \Lambda < 1 \times 10^{-3} \text{ and } La_t > 10, \\ G_l(\sigma) & \text{otherwise.} \end{cases} \quad (14)$$

These thresholds for La_t and Λ are somewhat arbitrary and more simulations are needed to assess them (as well as potential impacts of sharp thresholds on prognostic models). However, since this region of the La_t - Λ parameter space is far from the bulk of the joint PDF, we do not focus on precise values for now.

With $G_k(\sigma)$ defined we can base the next steps on Eq. (6), of which the only unknown is \mathcal{E} . We set out to estimate \mathcal{E} by fitting its value so as to minimize the error between $K(\sigma)$ given by Eq. (6) and the eddy diffusivity calculated via our optimization method (shown for selected cases in Fig. 5). We do this in two different ways: (i) we fit \mathcal{E} based only on data for the surface layer (\mathcal{E}^{sc} , where we take the surface layer to be the upper 10% of the OSBL) and (ii) we fit \mathcal{E} based on the entire OSBL (\mathcal{E}^{OSBL}). The rationale behind i is to focus on the modification of MOST relations by \mathcal{E} , which acts to decrease vertical gradients near the surface [given in nondimensional form by $\phi(z/L_o)$] through stronger vertical mixing. The reasoning behind ii is to focus on the impact on the vertical transport and mixing due to large eddies in the flow.

Results for approaches i and ii are shown in Figs. 8a and 8b, respectively. In both cases the largest enhancements to the eddy diffusivity happen for regimes that fall in the Langmuir-dominated region, as expected. Larger magnitudes are found when focusing on the surface layer for fitting (approach i), coinciding with the region where the Stokes drift has the largest shear. Note that clearly $\mathcal{E} > 1$ for the Pure Convection regime in both panels ($\Lambda \rightarrow \infty$, $La_t \rightarrow \infty$). This is most likely due to that regime being outside the range of validity of MOST measurements.

There is a general trend of \mathcal{E} to increase with decreasing La_t , which is expected given that this indicates stronger Langmuir circulations. However, for both \mathcal{E}^{sc} and \mathcal{E}^{OSBL} the trend is broken for the Neutral Swell case. Nonmonotonic dependence on La_t has been observed before for swell cases (McWilliams et al. 2014) and it may be due to the larger Stokes drift

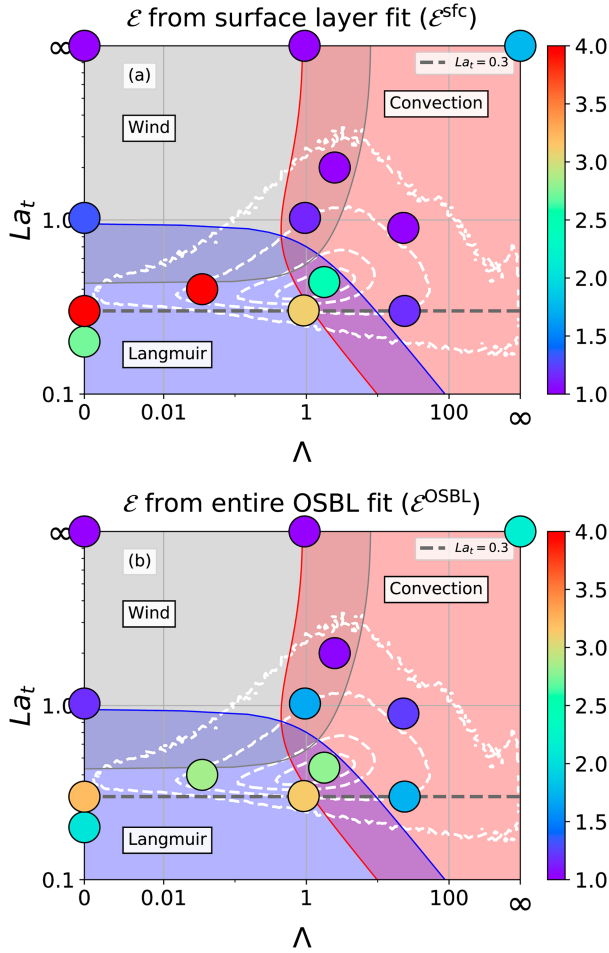


FIG. 8. The \mathcal{E} estimated by fitting Eq. (6) against $K(\sigma)$ obtained via the optimization method plotted as colored circles on top of the La_t - Λ parameter space.: showing (a) results for the fit using only the surface layer and (b) results for the fit using the entire OSBL.

penetration in this regime (by a factor of 2; see Table 3), which translates to a smaller shear at the surface. The use of the surface layer Langmuir number La_{SL} mitigates this effect (not shown), which is in line with previous studies indicating that La_{SL} may be more effective at capturing certain Langmuir effects (Harcourt and D'Asaro 2008). This should be especially true for broadband spectra, which we chose not to include in this study.

To compare our fitted coefficients with literature estimates we plot Fig. 9, which shows different formulations for \mathcal{E} in the vertical axes and $\mathcal{E}^{\text{OSBL}}$ in the horizontal axes. The chosen estimates of \mathcal{E} are those from Smyth et al. (2002), Harcourt and D'Asaro (2008), Takaya et al. (2010), Van Roekel et al. (2012) and Reichl et al. (2016) (see the appendix for details about their implementation), shown in Figs. 9a–e, respectively. The formulations by Harcourt and D'Asaro (2008) and Van Roekel et al. (2012) are based on empirical formulations for the averaged vertical velocity variance in the OSBL ($\overline{w'^2}$) (the overline indicating vertical average within the boundary

layer). Under such conditions the enhancement of vertical velocity variance (compared with neutral and waveless conditions; Li et al. 2005) is generally accepted to be the square of the eddy diffusivity enhancement \mathcal{E} since it is assumed that $u_s \sim \langle w'^2 \rangle^{1/2}$ in Eq. (6) (Reichl et al. 2016; Li et al. 2019).³

From Fig. 9 we see that the literature estimates somewhat capture the general trend of \mathcal{E} , although most of the formulations tend to underestimate \mathcal{E} relative to $\mathcal{E}^{\text{OSBL}}$. Estimates by Smyth et al. (2002), Harcourt and D'Asaro (2008), and Van Roekel et al. (2012) have roughly half of the points outside of the 30% error lines, while Reichl et al.'s (2016) formulation is clearly the one that matches our results the most. Note that \mathcal{E} for the swell regime appears to be better represented by formulations that consider La_{SL} (Figs. 9b,d,e) than formulations that use La_t (Figs. 9a,c). The largest deviation for the swell case happens for Smyth et al.'s (2002) formulation, which predicts $\mathcal{E} \approx 10$, while the fitted value is $\mathcal{E}^{\text{OSBL}} \approx 2$. This result provides further evidence that La_{SL} may be preferred in comparison with La_t .

It has been demonstrated that $\langle w'^2 \rangle$ scales with $\text{La}_{\text{SL}}^{-4/3}$ (which is consistent with a Langmuir-turbulence-dominated turbulent dissipation; Harcourt and D'Asaro 2008), while it seems that other flow metrics scale with $\text{La}_{\text{SL}}^{-2}$ (McWilliams et al. 2014), raising the question of which scaling is more appropriate for the eddy diffusivity enhancement \mathcal{E} . Among the \mathcal{E} formulations investigated here, only those by Harcourt and D'Asaro (2008) and Takaya et al. (2010) (Figs. 9b,c) derive from the $\text{La}_{\text{SL}}^{-4/3}$ scaling for vertical velocity variance. From Fig. 9 it does not seem that these formulations produce significantly different results than the other ones, and a more thorough examination is needed to further investigate this issue, which we leave for future studies.

Moreover, it has been pointed out that Langmuir cells tend to affect neutral simulations more than strongly convective ones (Li and Fox-Kemper 2017), which translates into a Λ -dependent \mathcal{E} formulation [i.e., $\mathcal{E}(\text{La}_t, \Lambda)$]. The only model that includes such a dependence is the one by Smyth et al. (2002), and it does not appear to match $\mathcal{E}^{\text{OSBL}}$ in convective regimes better than other models (based on Fig. 9). To further investigate this Λ dependence we have fitted various different ad hoc formulations for \mathcal{E} (that included both a La_t and a Λ dependence) against both \mathcal{E}^{sfc} and $\mathcal{E}^{\text{OSBL}}$. While the fitted coefficients reveal a clear dependence of \mathcal{E}^{sfc} on Λ , results for $\mathcal{E}^{\text{OSBL}}$ are inconclusive. Specifically, when fitting for $\mathcal{E}^{\text{OSBL}}$, there is an extremely high uncertainty level for every coefficient that impacts Λ . This result either indicates that a Λ dependence is unnecessary for $\mathcal{E}^{\text{OSBL}}$ (which would raise the question of why this is the case for $\mathcal{E}^{\text{OSBL}}$ but not \mathcal{E}^{sfc}) or it may simply be a result of not having enough data points for the fit. More extensive surveys are

³ An implicit assumption needed to go from $\langle w'^2 \rangle$ formulations to \mathcal{E} formulations is that Langmuir turbulence and convection do not affect the length scale of mixing relative to a pure wind stress (neutral waveless) regime. An alternative scaling would require that an integral time scale (Taylor 1922) be unaffected if one defines the eddy diffusivity on the basis of velocity and time scales, as opposed to velocity and length scales.

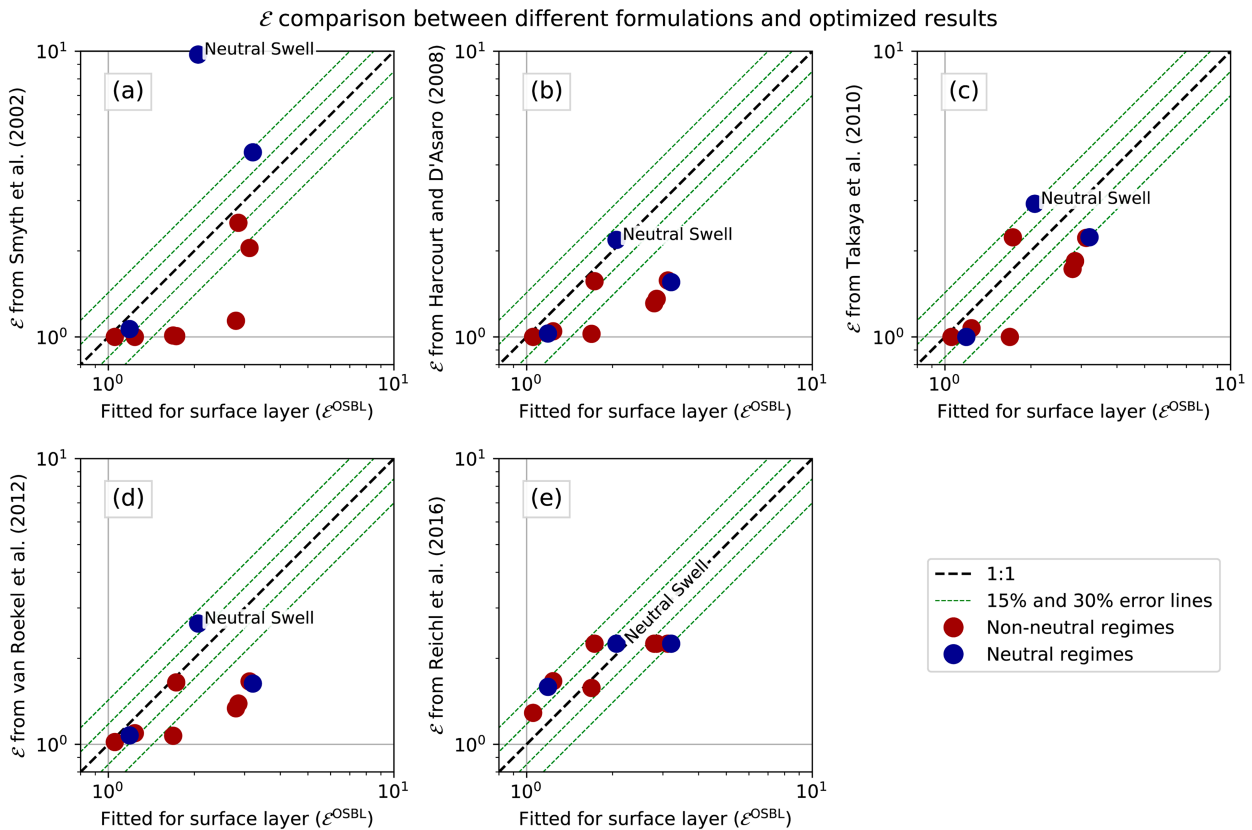


FIG. 9. Estimates for the enhancement factor \mathcal{E} from different formulations compared with its fitted value for our results $\mathcal{E}^{\text{OSBL}}$. Compared formulations are those from (a) Smyth et al. (2002), (b) Harcourt and D'Asaro (2008), (c) Takaya et al. (2010), (d) Van Roekel et al. (2012), and (e) Reichl et al. (2016). Also shown are the 1:1 line (dashed black) and lines corresponding to 15% and 30% error (dashed green). Note that \mathcal{E} is a function of depth in Reichl et al.'s (2016) formulation, and we report its maximum value here.

needed to further investigate this issue. Moreover none of the fitted expressions obtained in this procedure (either for \mathcal{E}^{sc} or $\mathcal{E}^{\text{OSBL}}$) is reported here since they did not significantly improve results relative to the formulations available in the literature.

In the rest of the paper, we focus on \mathcal{E} obtained using the entire OSBL ($\mathcal{E}^{\text{OSBL}}$) in order to concentrate on the enhanced mixing effects of large eddies. Furthermore, it should be noted that final results were observed to be similar regardless of which \mathcal{E} estimation was chosen.

5. Implications for modeling

A few key differences become clear when comparing our results to the curves used by models. The first is that models generally underestimate the eddy diffusivity magnitudes compared to our method (see Fig. 5), which is not surprising since our method maximizes $K(z)$. Furthermore, much of the difference in $K(\sigma)$ between models and our results appears in the middle of the OSBL and seems to be related to a difference in shape. In particular, whenever waves are present $K(\sigma)$ assumes a shape that is clearly different from a cubic polynomial (see Fig. 6a, which shows that our shapes have a more

pronounced peak that is closer to the surface when compared to a cubic polynomial). This implies that much of the discrepancies between our results and models can be reduced in a straightforward way simply by considering an alternative shape in wavy regimes.

Our results also suggest that the magnitude of $G_s(\sigma)$ should depend on the magnitude of surface buoyancy fluxes, and not just its presence, as is common with previous models [see Eq. (7) and Fig. 7]. Furthermore, based on the regimes on the $\Lambda = 0$ line in Fig. 4, $G_s(\sigma)$ should also depend on whether or not the ocean has waves. Some studies have identified influences on nondiffusive transport in KPP-like models whenever Langmuir circulations are present (Yang et al. 2015; Chamecki et al. 2019) and our results confirm that in a more systematic manner since profiles for $G_s(\sigma)$ are, through the definition of our optimization method, as small as they can be.

Moreover, $G_s(\sigma)$ shapes obtained by our method are clearly different from the cubic shape used by previous models, especially in the surface layer. This is no surprise since the assumption of a cubic shape for $G_s(\sigma)$ is essentially a pragmatic one and our results further indicate that the shapes of $K(\sigma)$ and $G_s(\sigma)$ need not be the same. Finally, our results point to $G_e(\sigma)$ contributions being small throughout the parameter space

(see Fig. 4), which justifies the community practice of neglecting that flux component in KPP.

In summary, these results indicate that (i) a change in the function $G_k(\sigma)$ for another shape in wavy regimes may be beneficial, (ii) $G_s(\sigma)$ should change magnitude depending on La_t and Λ , (iii) $G_s(\sigma)$ should also have a different shape than the cubic shape $G_n(\sigma)$, and (iv) $G_e(\sigma)$ may be neglected for now. We will explore these aspects in the next section.

6. Changes to KPP

On the basis of the discussion from the previous section we consider modifications to existing wave-aware KPP formulations and explore their impact on modeled fluxes.

a. Eddy diffusivity

For the purposes of implementation, we use $G_k(\sigma)$ as defined in Eq. (14) with the empirical function $G(\sigma)$ as defined in Eq. (13). More information on implementing this shape and an alternative polynomial fit can be found in the appendix. We also report results using only \mathcal{E} from Reichl et al. (2016), which we refer to as \mathcal{E}^{R16} from now on. This is done for the sake of simplicity, since the bulk results reported are very similar independently of the enhancement factor formulation [the exception being simulation Neutral Swell using \mathcal{E} from Smyth et al. (2002)]. This is an indication that, despite the differences in \mathcal{E} seen in Fig. 9, most of the differences in results come from changing the shapes $G_k(\sigma)$ and $G_s(\sigma)$ (to be detailed in the next section).

b. Nondiffusive flux

According to the previous discussions, the nondiffusive shape function should have a dependence on waves and surface buoyancy fluxes (characterized by La_t and Λ , respectively). This dependence can be introduced in a simple way as

$$G_s(\sigma) = [\text{Langmuir} + \text{Convection}]g_s(\sigma), \quad (15)$$

$$\text{Langmuir} = \mathcal{L}_1 [1 - H(La_t - La_c)], \quad \text{and} \quad (16)$$

$$\text{Convection} = \mathcal{C}_1 H(\Lambda) \frac{\{1 + \text{erf}[\mathcal{C}_2(\Lambda - \Lambda_c)]\}}{2}, \quad (17)$$

where we impose that $\Lambda_c = \kappa$ (which happens when $u_* = w_*$). Furthermore, since we do not have enough information about the transition between no waves and weak waves, we somewhat arbitrarily choose a step transition that happens for $La_c = 10$ ($u_* = 100u_0^*$). This additive formulation for Langmuir and convective effects is an initial step, but, as indicated by Fig. 4a, interactions between both processes are possible and should be explored in the future.

We base ourselves on Fig. 6c and define $g_s(\sigma) = G_s(\sigma)/B^*$, with B^* being a rescaling factor chosen so that $\max[g_s(\sigma)] = 0.15$. This arbitrary rescaling is done so that the magnitude of $g_s(\sigma)$ roughly matches that of $G_n(\sigma)$ (traditionally used in KPP), which facilitates comparisons. Details on implementing this alternative shape can be found in the appendix along with

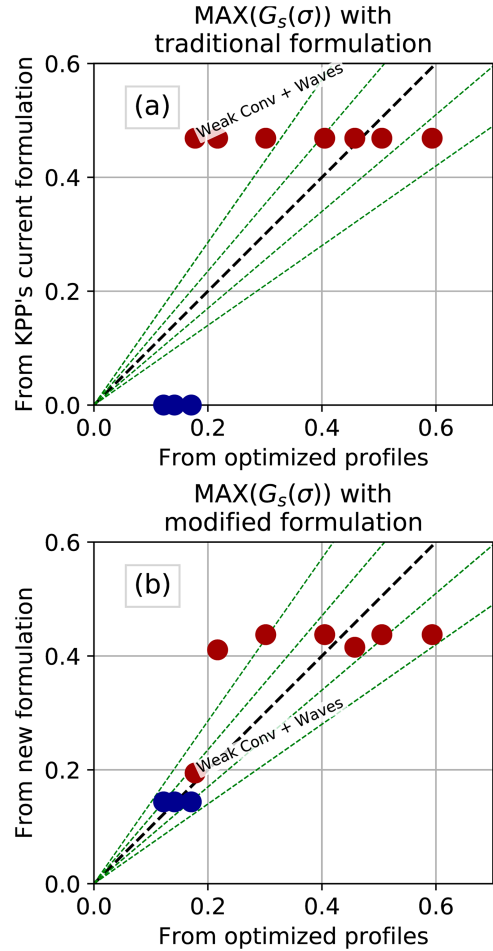


FIG. 10. Comparison between the nondiffusive component shape function $G_s(\sigma)$ with and without considering Langmuir effects in its formulation as quantified by their maximum value in the OSBL. The horizontal axis shows the values for the results of the optimization, and vertical axes show results using (a) KPP's original formulation and (b) Eq. (15). Also shown are the 1:1 line (dashed black) and lines corresponding to 15% and 30% error (dashed green).

polynomial functions to approximate the relevant curves. Furthermore, note that the Heaviside function on the Convection term ensures that the contributions from convection are null in neutral and stable regimes, which is also common practice with the original KPP.

A fit of Eqs. (15)–(17) using all wavy regimes yields the values $\mathcal{L}_1 = 0.95$, $\mathcal{C}_1 = 1.95$, and $\mathcal{C}_2 = 1.82$. A comparison between diagnosed $G_s(\sigma)$ from our optimization method and from Eqs. (15)–(17) is shown in Fig. 10b, where the chosen measure is the maximum value of $G_s(\sigma)$ in the OSBL (which in our formulation happens at around $\sigma \approx 1/2$). Roughly half of the regimes fall within the 15% error lines. For the sake of reference we also show our optimized profiles against the currently used KPP formulation in Fig. 10a. A comparison between Figs. 10 and 10b reveals that including Langmuir effects in the formulation for $G_s(\sigma)$ significantly improves results, further indicating the importance of Langmuir circulations for nondiffusive

fluxes. Note that the goal of this comparison is not to emphasize that our fitted expression is a better match to the diagnosed values, but to illustrate that Langmuir turbulence effects need to be included in the nondiffusive flux formulation of KPP in order to faithfully represent wavy regimes.

The values of \mathcal{L}_1 and \mathcal{C}_1 suggest that waves can have an impact on nondiffusive fluxes that is approximately half of that for strong convection. For a representative oceanic regime [say Simulation Weak Conv + Wind-Wave Eq., where Eqs. (15)–(17) and our optimization differ by only 10% on their estimate of $G_s(\sigma)$], these values predict that around 35% of the nondiffusive fluxes are due to Langmuir circulations, pointing to the need to include this effect in KPP.

c. Passive scalar flux comparisons

We show results for the total turbulent flux and each individual component F_D and F_{ND} in Fig. 11 for simulation Joint PDF Peak, where we compare results from two different KPP formulations (dashed lines) with results from our optimized method (solid lines). Figures 11a and 11c show results from the original KPP formulation using \mathcal{E}^{R16} as dashed lines while Figs. 11b and 11d show results from our modified KPP as dashed lines. Top panels show fluxes for SFTs, where it is clear that much of the error happens in the surface layer due to the parameterization of the diffusive fluxes. The diffusive term also artificially produces a bump in the entrainment layer that is small using our proposed formulation but very significant when using the original KPP formulation. It is challenging to represent diffusive fluxes in these regions due to the large gradients, which enhances small errors in the eddy diffusivity. However, the middle of OSBL is generally well represented by the diffusive term in both formulations. The nondiffusive terms match relatively well using our new formulation that takes Langmuir into account (Fig. 11b), but there is significant mismatch using the original KPP formulation (Fig. 11a), especially in the surface layer. In general our modified formulation appears to be more accurate than the traditional one.

Figures 11c and 11d show results for the same simulation but for EFTs. Fluxes using our proposed formulation (Fig. 11d) are reasonably well represented until about $\sigma = 1/2$ [even considering the error introduced in neglecting $G_e(\sigma)$; dashed blue line]. Model results using the original KPP formulation (Fig. 11d) underdiagnose the flux in the same region. The diffusive flux is poorly represented in both cases in the entrainment due again to the very large gradients in this region, however, results are significantly worse using the original KPP formulation (Fig. 11c).

Figure 11 is predominantly representative of the other simulations studied here: most of the error happens in regions of large gradients (i.e., the surface and entrainment layers) while the middle of the OSBL is better represented. This is true for both KPP formulations. With that in mind we avoid analyzing each simulation in detail by calculating the mean normalized error in the OSBL δF defined as

$$\delta F = \frac{1}{\langle w'c' \rangle_b} \left[\int_0^1 (F_{LES} - F_{KPP})^2 d\sigma \right]^{1/2}, \quad (18)$$

where F is the total turbulent flux (either from LES or using KPP) and $\langle w'c' \rangle_b$ is a normalization factor equal to the absolute value of the surface flux for SFTs and the entrainment flux for EFTs.

We apply Eq. (18) to the results of three KPP formulations: formulation A, using the traditional KPP formulation with \mathcal{E}^{R16} (same formulation used in the left panels of Fig. 11); formulation B, using our modified KPP formulation [Eqs. (14) and (15)] with \mathcal{E}^{R16} ; and formulation C, using our modified KPP formulation with \mathcal{E}^{OSBL} (same formulation used in the right panels of Fig. 11). Thus, the difference from formulations A to B is simply the formulation of $G_k(\sigma)$ and $G_s(\sigma)$. From formulations B to C we change only \mathcal{E}^{R16} to the OSBL-fitted \mathcal{E}^{OSBL} , therefore assessing the loss in accuracy from using a formulaic estimate of \mathcal{E} instead of an optimized one.

Results for δF can be seen in Fig. 12 for formulations A (left panels), B (center panels), and C (right panels). Figures 12a–c show δF for SFTs and Figs. 12d–f show δF for EFTs. Only wavy simulations are shown with nonneutral simulations shown in red and neutral simulations in blue. From comparing Figs. 12a and 12b [whose only differences are $G_k(\sigma)$ and $G_s(\sigma)$] we can see that replacing the commonly used cubic function for the proposed formulations somewhat improves the representation of SFT fluxes, although the difference is small. However, the improvement for EFT fluxes is much more significant (Figs. 12d,e; note the difference in the vertical axis between the top row and the one below it). Furthermore, Fig. 12d reveals that the traditional KPP is significantly worse at diagnosing EFT fluxes than SFT fluxes. Such a large discrepancy between EFTs and SFTs does not happen using the shape functions proposed in this paper.

Analyzing the transition between the central panels of Fig. 12 and the right panels, we see that δF decreases only slightly when going from formulation B to C (for both SFTs and EFTs). This indicates that modeling the enhancement factor \mathcal{E} with a simple formulation is not a major source of error and most of the discrepancies between the diagnosed KPP fluxes and those from LES can be accounted for by the shape functions used. Such a result suggests that the accuracy of KPP can be significantly improved simply by changing the formulations for $G_k(\sigma)$ and $G_s(\sigma)$.

d. Potential temperature flux comparisons

We dedicate this section to analyzing the effect of our modifications when diagnosing potential temperature fluxes with KPP for the sake of completeness. We assume that $K(\sigma)$ and $G_s(\sigma)$ are the same for passive scalars and temperature, and we use their profiles to reconstruct the turbulent fluxes from the LES-measured mean potential temperature gradients. Results for the turbulent flux separation via this method can be seen for simulation Joint PDF Peak in Figs. 11e and 11f. As is the case for passive scalars, the new formulation appears to more accurately capture both the total flux and each separate component than the traditional formulation.

Since results for simulation Joint PDF Peak are representative of other regimes, we also apply Eq. (18) to potential temperature to obtain a bulk error measure. Results of δF for temperature

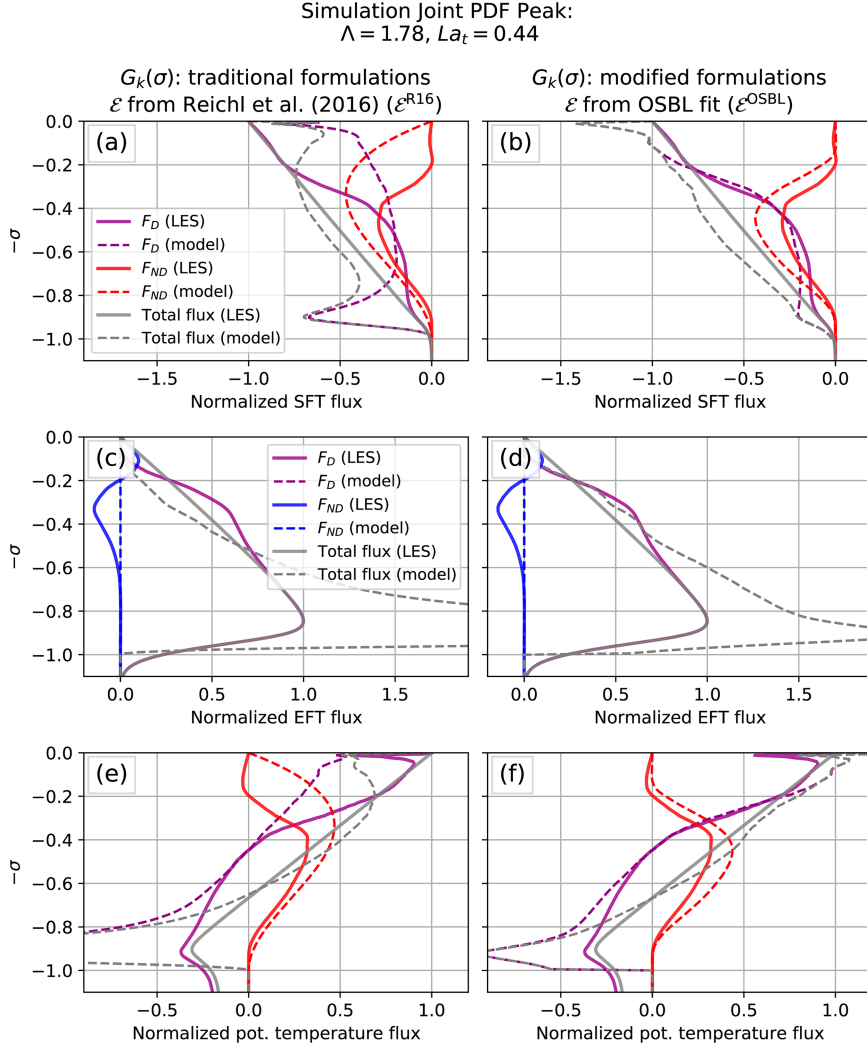


FIG. 11. Normalized turbulent fluxes for (a),(b) SFTs; (c),(d) EFTs; and (e),(f) temperature flux for simulation Joint PDF Peak. Solid lines are LES results, and dashed lines are results from KPP formulations. (left) Model results obtained using the traditional formulation for $G_k(\sigma)$ and $G_s(\sigma)$ and enhancement factor from Reichl et al.'s (2016) formulation. (right) Model results obtained with the modified formulation introduced in this paper. Gray lines are the full turbulent flux, red lines are nondiffusive fluxes due to surface processes, and blue lines are nondiffusive fluxes due to entrainment processes.

are shown in Figs. 12g–i, where each column corresponds to results using a different formulation as indicated at the top of the figure. We again see that results are similar to those for passive scalars: the overall error is significantly reduced when switching from the cubic shape to the one introduced in this work, and the formulation for ε does not appear to introduce major discrepancies.

Even though potential temperature was never considered in any of the analyses up to this point, the accuracy of the flux representation is similar to that of the passive scalars (Figs. 12a–d). This result builds confidence in our assumption of universality of $K(\sigma)$ and $G_s(\sigma)$ profiles and further provides evidence that changing the formulation of $G_k(\sigma)$ and $G_s(\sigma)$ in KPP may be beneficial.

7. Conclusions

Efforts to adapt KPP to Langmuir turbulence flows have concentrated on two different effects: the modification of the eddy diffusivity profiles to account for increased mixing (Smyth et al. 2002) and the modification of the OSBL depth calculation to account for increased entrainment at the mixed layer base (Li and Fox-Kemper 2017). These efforts are complimentary and both are necessary to correctly represent OSBL effects in large-scale models. In this work we assumed the OSBL depth to be known and focused on a more general determination of both $K(z)$ and $F_{ND}(z)$ (instead of focusing only on $K(z)$ as most previous studies). In particular we investigated the question of how should KPP profiles be modified to better account for the effects of Langmuir

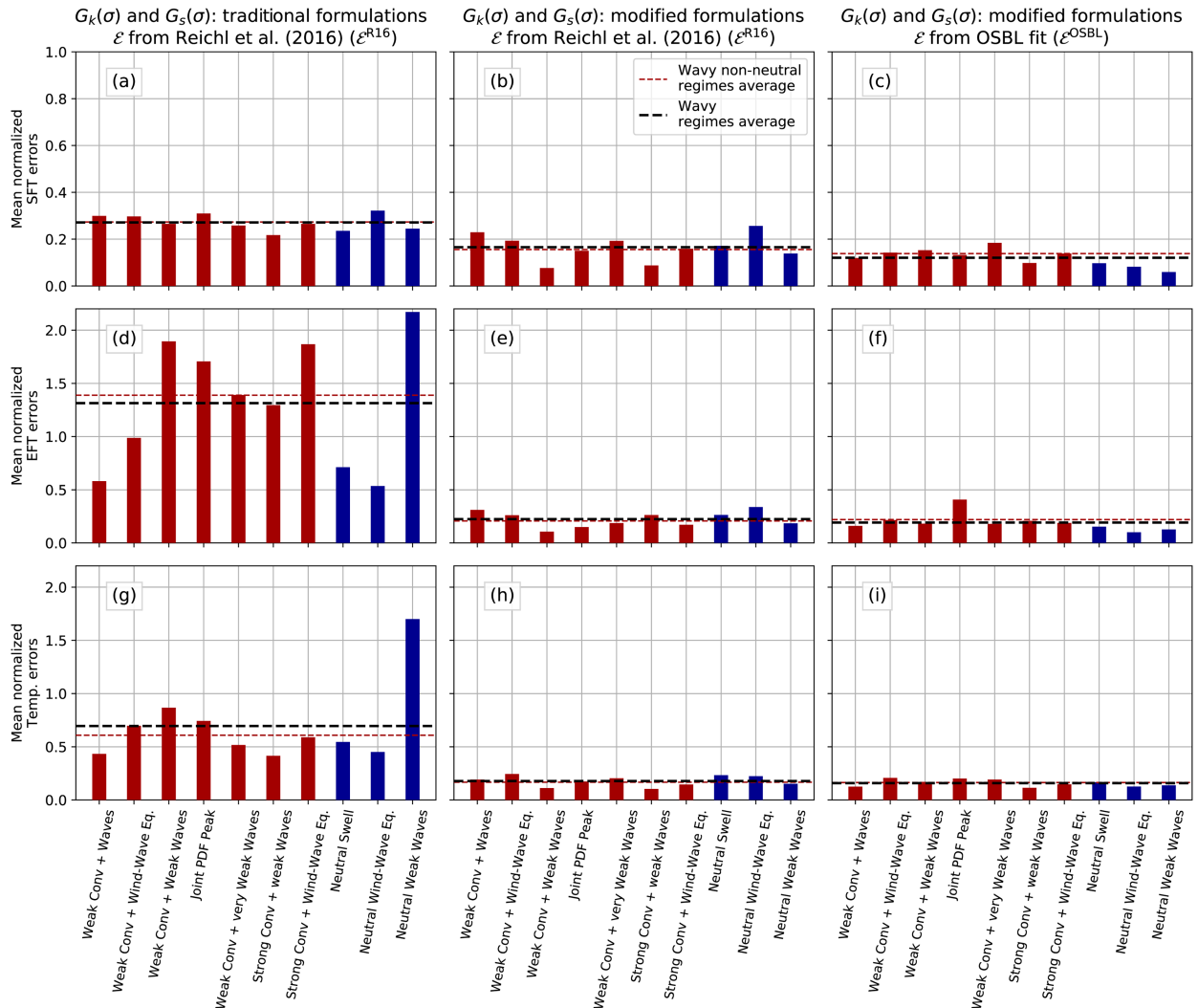


FIG. 12. Mean normalized error δF for each simulation with waves: (a)–(c) results for SFTs, (d)–(f) results for EFTs, and (g)–(i) results for temperature. Each column shows results for the total turbulent flux error calculated using a different formulation with differences in $G_k(\sigma)$, $G_s(\sigma)$ and in the estimation of \mathcal{E} , as indicated at the top of the figure.

turbulence. In most previous works in this line, the bulk of the proposed modifications to the KPP profiles consisted in enhancing the eddy diffusivity (Li et al. 2019). The main conclusion of this work is that other modifications to the profiles are likely needed in addition to the eddy-diffusivity enhancement.

First, the formulation of the nondiffusive fluxes F_{ND} should be changed to account for Langmuir circulations. In previous KPP versions the nondiffusive flux formulation depends solely on the presence of a surface destabilizing buoyancy flux (Large et al. 1994; Sullivan and McWilliams 2010; Smyth et al. 2002). However, we showed that the smallest F_{ND} necessary to reproduce observed fluxes using KPP in wavy regimes without buoyancy fluxes is still significant. As an example, in a neutral regime in wind–wave equilibrium ($La_t = 0.3$) where large flow structures are likely to come from Langmuir circulations, F_{ND} accounts for at least 40% of the flux in the middle

of the OSBL (see Fig. 3). We proposed an alternative formulation for $G_s(\sigma)$ [given by Eqs. (15)–(17)] in which the effects of Langmuir circulations and convection are additive. A fit of the coefficients to LES data suggests that waves can account for approximately one-third the magnitude of nondiffusive fluxes in convective regimes, but further investigations are needed for a more precise number.

Second, changing the shapes of both the eddy diffusivity and the nondiffusive F_{ND} fluxes is likely to be beneficial since our results show that both assume a shape that is different from the commonly used cubic polynomial (O'Brien 1970; Large et al. 1994). Our results also show that shapes for F_{ND} and the eddy diffusivity are different from each other, which is different from previous KPP versions.

Furthermore, while most discrepancies between KPP-diagnosed fluxes and LES-measured ones in our results come from the choice of the shape function, the lack of consensus

on the wave-driven flux enhancement still needs to be remedied. While the proposed changes in this paper would also extend this influence to the nondiffusive flux term, there are still questions regarding the diffusivity enhancement factor \mathcal{E} . In particular some of the unknowns are how \mathcal{E} should scale with the Langmuir number La_t (Harcourt and D'Asaro 2008; McWilliams et al. 2014) and whether or not \mathcal{E} depends on the stability Λ (Li and Fox-Kemper 2017). Our results point toward the Langmuir number being more important than Λ , but more investigations are needed to explore these issues.

Note that we performed a diagnostic analysis of OSBL turbulent fluxes in which KPP calculations are carried out with averaged profiles from LES, which assesses the accuracy of modeling assumptions rather than model performance. While diagnostic studies are important, especially in first studies such as the present paper, the main goal of KPP is to provide predictive capabilities to large-scale models. Therefore, our results should also be assessed prognostically (Pope 2000, section 13.4.6), by using KPP formulations to advance mean profiles in time. This investigation, however, is outside the present scope since it would require many extra comparisons and a thorough investigation of other aspects of KPP (such as the OSBL depth estimation and possibly different formulations for momentum), being more suited for a dedicated future study.

Our simulations do not contain several effects that could complicate analyses. These include wind-wave misalignment (Van Roekel et al. 2012) and swell effects on wind-wave equilibrium (McWilliams et al. 2014), as well as breaking waves (Sullivan and McWilliams 2010). It is possible that the use of broadband wave spectra reveals a dependence of the $K(\sigma)$ and $g_s(\sigma)$ profiles on the Stokes drift, but, since this investigation requires a significant number of extra simulations, we chose not to pursue that possibility here. We have also considered only one value for the Coriolis parameter, and it is possible that varying this parameter (as well as including the aforementioned effects) may change the profiles reported here, especially for shear-dominated regimes. These extra complexities were beyond the scope of this paper and are left for future studies.

Acknowledgments. This research was made possible by a grant from the Gulf of Mexico Research Initiative. The authors also thank Dr. Qing Li for providing the data for the joint PDF used in the parameter space plots.

Data availability statement. Data are publicly available through the Gulf of Mexico Research Initiative Information and Data Cooperative [GRIIDC; <https://data.gulfresearchinitiative.org/data/R5.x283.000:0008> (doi:10.7266/JRFXRNA9)].

APPENDIX

KPP Implementation

Based on the fact that the waves in our regimes are wind aligned and u_{ref}^s is small, we are able to simplify some of the formulations for \mathcal{E} from the literature used for the

purposes of this work. Formulations by Smyth et al. (2002)⁴ and Takaya et al. (2010) were used exactly as they appear in their original papers. The formulation for Harcourt and D'Asaro (2008) used here is based on their equation for the vertical variance and can be written as

$$\mathcal{E}_{H1} = a_1 + a_2 \text{La}_{SL}^{-4/3}, \quad (\text{A1})$$

$$\mathcal{E}_{H2} = a_3 + a_4 \exp(-a_5 \text{La}_{SL}), \quad \text{and} \quad (\text{A2})$$

$$\mathcal{E} = \left[\frac{1}{0.64} \max(\mathcal{E}_{H1}, \mathcal{E}_{H2}) \right]^{1/2}, \quad (\text{A3})$$

with coefficients $a_1 = 0.398$, $a_2 = 0.48$, $a_3 = 0.64$, $a_4 = 3.5$, $a_5 = 2.69$.

The formulation for Van Roekel et al.'s (2012) enhancement factor is also based on their equation for the average vertical velocity variance and it can be written as

$$\mathcal{E} = [1 + (b_1 \text{La}_{SL})^{-2} + (b_2 \text{La}_{SL})^{-4}]^{1/2}, \quad (\text{A4})$$

with coefficients $b_1 = 1.5$ and $b_2 = 5.4$.

The formulation for Reichl et al.'s (2016) enhancement factor can be written as

$$\mathcal{E} = 1 + (\mathcal{E}' - 1) \frac{G_n(\sigma)}{\max[G_n(\sigma)]} \quad \text{and} \quad (\text{A5})$$

$$\mathcal{E}' = \min(2.25, 1 + \text{La}_{SL}^{-1}). \quad (\text{A6})$$

To make future investigations easier for the reader, we included the empirical shape profiles $G_i(\sigma)$ and $g_s(\sigma)$ in a public Zenodo repository (Chor et al. 2020a) as a comma-separated value file. Furthermore, the same file is available on the GRIIDC website (see data availability statement).

We also report polynomial fits of the same curves. The fit for the shape function $G_s(\sigma)$ was performed with a weighting function $\mathcal{W}(\sigma) = |dC_{SFT}^*/d\sigma| + |dC_{EFT}^*/d\sigma|$, where $dC_i^*/d\sigma$ is the mean gradient of the i th scalar (SFT or EFT) normalized such that the maximum gradient is unity in the OSBL for any given simulation. $\mathcal{W}(\sigma)$ depends on the depth and it is an average between all wavy regimes. The rationale for $\mathcal{W}(\sigma)$ is that the precise value of $K(\sigma)$ [and therefore $G_i(\sigma)$] is more important in regions with large gradients. $\mathcal{W}(\sigma)$ generally gives more weight for values close to the surface and close to $\sigma = 1$, since these regions generally exhibit larger gradients.

The lowest degree polynomial that produces reasonable results for $G_i(\sigma)$ is a sextic polynomial, which satisfies the usual constraints for KPP, namely, $G_k(\sigma = 0) = G_k(\sigma = 1) = 0$, $dG_k/d\sigma = 1$ at the surface and $dG_k/d\sigma = 0$ at $\sigma = 1$ (O'Brien 1970). The result of the fit can be seen in Fig. A1a as a dashed brown line, and its formula is

⁴ In Smyth et al. (2002) the convective velocity w_* is defined differently from our definition. However, this appears to be a typographical error because none of the other equations in their paper reflect that alternative definition, and we maintain the original formulation with the reported values for the coefficients exactly while still using our definition of w_* .

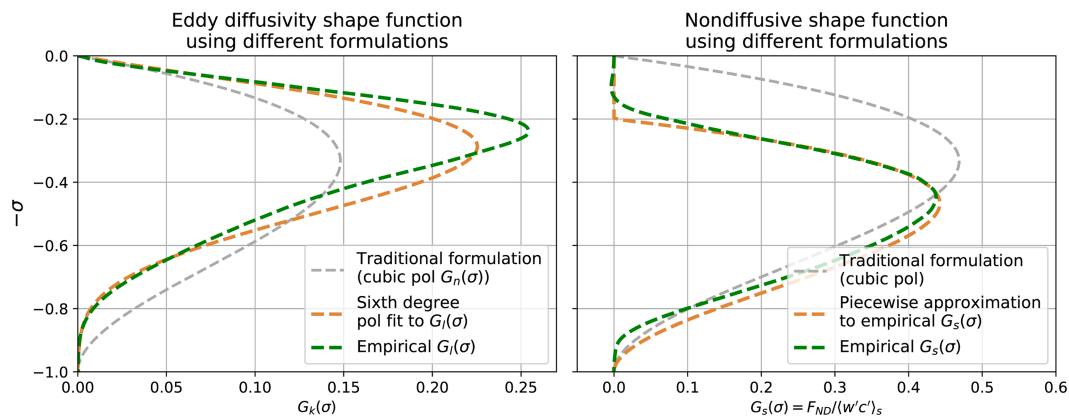


FIG. A1. (a) Eddy diffusivity shape functions for wavy conditions $G_l(\sigma)$. The dashed green line shows the empirical curve obtained by averaging profiles from all simulations and imposing MOST compliance. The dashed brown line shows the weighted polynomial fit (using \mathcal{W}) to this curve, and the dashed gray line is KPP's original cubic polynomial. (b) As in (a), but for the surface-driven nondiffusive shape function $G_s(\sigma)$.

$$G_l(\sigma) = \sigma(1-\sigma)^2[1 + c_4\sigma + c_5(\sigma + \sigma^2) + c_6(3\sigma + 2\sigma^2 + \sigma^3)], \quad (\text{A7})$$

with the fitted coefficients $c_4 = 45$, $c_5 = -33$, and $c_6 = 9$. Also shown are the original empirical curve and the traditional cubic curve for reference. Notice that, due to the weighting factor, the polynomial fit is very accurate close to $\sigma = 1$ and the surface, but significantly less so in the middle of the OSBL. In our tests, this level of accuracy already produces results that are virtually identical to those produced using the true empirical function, but might be subpar for applications with sharper gradients away from the boundaries.

Based on $G_s(\sigma)$ profiles for wavy regimes (see Fig. 6c), we choose $g_s(\sigma)$ as being a piecewise function that can be written with the aid of a Heaviside function $H()$ as

$$g_s(\sigma) = 2(\sigma - 0.2)(1 - \sigma)^2 H(\sigma - 0.2), \quad (\text{A8})$$

valid for $0 \leq \sigma \leq 1$. As an illustration we show $G_s(\sigma)$ for simulation Strong Conv + Wind-Wave Eq. in Fig. A1b as a dashed brown line.

REFERENCES

- Belcher, S. E., and Coauthors, 2012: A global perspective on Langmuir turbulence in the ocean surface boundary layer. *Geophys. Res. Lett.*, **39**, <https://doi.org/10.1029/2012GL052932>.
- Bou-Zeid, E., C. Meneveau, and M. Parlange, 2005: A scale-dependent Lagrangian dynamic model for large eddy simulation of complex turbulent flows. *Phys. Fluids*, **17**, 025105, <https://doi.org/10.1063/1.1839152>.
- Chamecki, M., C. Meneveau, and M. B. Parlange, 2008: A hybrid spectral/finite-volume algorithm for large-eddy simulation of scalars in the atmospheric boundary layer. *Bound.-Layer Meteor.*, **128**, 473–484, <https://doi.org/10.1007/s10546-008-9302-1>.
- , T. Chor, D. Yang, and C. Meneveau, 2019: Material transport in the ocean mixed layer: Recent developments enabled by large eddy simulations. *Rev. Geophys.*, **57**, 1338–1371, <https://doi.org/10.1029/2019RG000655>.
- Chen, B., D. Yang, C. Meneveau, and M. Chamecki, 2016: Effects of swell on transport and dispersion of oil plumes within the ocean mixed layer. *J. Geophys. Res. Oceans*, **121**, 3564–3578, <https://doi.org/10.1002/2015JC011380>.
- Chor, T., D. Yang, C. Meneveau, and M. Chamecki, 2018: A turbulence velocity scale for predicting the fate of buoyant materials in the oceanic mixed layer. *Geophys. Res. Lett.*, **45**, 11 817–11 826, <https://doi.org/10.1029/2018GL080296>.
- , J. McWilliams, and M. Chamecki, 2020a: Empirical shapes for the publication “Modifications of the K -profile parameterization with nondiffusive fluxes for wave effects.” Zenodo, <https://doi.org/10.5281/zenodo.4062665>.
- , J. C. McWilliams, and M. Chamecki, 2020b: Diffusive–nondiffusive flux decompositions in atmospheric boundary layers. *J. Atmos. Sci.*, **77**, 3479–3494, <https://doi.org/10.1175/JAS-D-20-0093.1>.
- Corrsin, S., 1975: Limitations of gradient transport models in random walks and in turbulence. *Turbulent Diffusion in Environmental Pollution*, F. Frenkiel and R. Munn, Eds., Advances in Geophysics, Vol. 18, Elsevier, 25–60, [https://doi.org/10.1016/S0065-2687\(08\)60451-3](https://doi.org/10.1016/S0065-2687(08)60451-3).
- Craik, A. D. D., and S. Leibovich, 1976: A rational model for Langmuir circulations. *J. Fluid Mech.*, **73**, 401–426, <https://doi.org/10.1017/S0022112076001420>.
- Deardorff, J., 1966: The counter-gradient heat flux in the lower atmosphere and in the laboratory. *J. Atmos. Sci.*, **23**, 503–506, [https://doi.org/10.1175/1520-0469\(1966\)023<0503:TCGHFI>2.0.CO;2](https://doi.org/10.1175/1520-0469(1966)023<0503:TCGHFI>2.0.CO;2).
- Grant, A. L. M., and S. E. Belcher, 2009: Characteristics of Langmuir turbulence in the ocean mixed layer. *J. Phys. Oceanogr.*, **39**, 1871–1887, <https://doi.org/10.1175/2009JPO4119.1>.
- Griffies, S. M., M. Levy, A. J. Adcroft, G. Danabasoglu, R. W. Hallberg, D. Jacobsen, W. Large, and T. Ringler, 2015: Theory and numerics of the community ocean vertical mixing (CVMix) project. CVMix Project Tech. Rep., 98 pp., <https://github.com/CVMix/CVMix-description/blob/master/cvmix.pdf>.
- Harcourt, R. R., and E. A. D’Asaro, 2008: Large-eddy simulation of Langmuir turbulence in pure wind seas. *J. Phys. Oceanogr.*, **38**, 1542–1562, <https://doi.org/10.1175/2007JPO3842.1>.

- Jayaraman, B., and J. G. Brasseur, 2018: The surprising transition in atmospheric boundary layer turbulence structure from neutral to moderately convective stability states and mechanisms underlying large-scale rolls. *arXiv*, 38 pp., <https://arxiv.org/abs/1807.03336>.
- Kaimal, J. C., J. C. Wyngaard, D. A. Haugen, O. R. Coté, Y. Izumi, S. J. Caughey, and C. J. Readings, 1976: Turbulence structure in the convective boundary layer. *J. Atmos. Sci.*, **33**, 2152–2169, [https://doi.org/10.1175/1520-0469\(1976\)033<2152:TSITCB>2.0.CO;2](https://doi.org/10.1175/1520-0469(1976)033<2152:TSITCB>2.0.CO;2).
- Large, W. G., J. C. McWilliams, and S. C. Doney, 1994: Oceanic vertical mixing: A review and a model with a nonlocal boundary layer parameterization. *Rev. Geophys.*, **32**, 363–403, <https://doi.org/10.1029/94RG01872>.
- , E. G. Patton, A. K. DuVivier, P. P. Sullivan, and L. Romero, 2019a: Similarity theory in the surface layer of large-eddy simulations of the wind-, wave-, and buoyancy-forced southern ocean. *J. Phys. Oceanogr.*, **49**, 2165–2187, <https://doi.org/10.1175/JPO-D-18-0066.1>.
- , —, and P. P. Sullivan, 2019b: Nonlocal transport and implied viscosity and diffusivity throughout the boundary layer in les of the southern ocean with surface waves. *J. Phys. Oceanogr.*, **49**, 2631–2652, <https://doi.org/10.1175/JPO-D-18-0202.1>.
- Li, M., C. Garrett, and E. Skillingstad, 2005: A regime diagram for classifying turbulent large eddies in the upper ocean. *Deep-Sea Res. I*, **52**, 259–278, <https://doi.org/10.1016/j.dsr.2004.09.004>.
- Li, Q., and B. Fox-Kemper, 2017: Assessing the effects of Langmuir turbulence on the entrainment buoyancy flux in the ocean surface boundary layer. *J. Phys. Oceanogr.*, **47**, 2863–2886, <https://doi.org/10.1175/JPO-D-17-0085.1>.
- , A. Webb, B. Fox-Kemper, A. Craig, G. Danabasoglu, W. G. Large, and M. Vertenstein, 2016: Langmuir mixing effects on global climate: WAVEWATCH III in CESM. *Ocean Modell.*, **103**, 145–160, <https://doi.org/10.1016/j.ocemod.2015.07.020>.
- , and Coauthors, 2019: Comparing ocean surface boundary vertical mixing schemes including Langmuir turbulence. *J. Adv. Model. Earth Syst.*, **11**, 3545–3592, <https://doi.org/10.1029/2019MS001810>.
- Marlatt, S., S. Waggy, and S. Biringen, 2012: Direct numerical simulation of the turbulent Ekman layer: Evaluation of closure models. *J. Atmos. Sci.*, **69**, 1106–1117, <https://doi.org/10.1175/JAS-D-11-0107.1>.
- McWilliams, J. C., P. P. Sullivan, and C.-H. Moeng, 1997: Langmuir turbulence in the ocean. *J. Fluid Mech.*, **334**, 1–30, <https://doi.org/10.1017/S0022112096004375>.
- , E. Huckle, J. Liang, and P. P. Sullivan, 2014: Langmuir turbulence in swell. *J. Phys. Oceanogr.*, **44**, 870–890, <https://doi.org/10.1175/JPO-D-13-0122.1>.
- Moeng, C.-H., and P. P. Sullivan, 1994: A comparison of shear-and buoyancy-driven planetary boundary layer flows. *J. Atmos. Sci.*, **51**, 999–1022, [https://doi.org/10.1175/1520-0469\(1994\)051<0999:ACOSAB>2.0.CO;2](https://doi.org/10.1175/1520-0469(1994)051<0999:ACOSAB>2.0.CO;2).
- O'Brien, J. J., 1970: A note on the vertical structure of the eddy exchange coefficient in the planetary boundary layer. *J. Atmos. Sci.*, **27**, 1213–1215, [https://doi.org/10.1175/1520-0469\(1970\)027<1213:ANOTVS>2.0.CO;2](https://doi.org/10.1175/1520-0469(1970)027<1213:ANOTVS>2.0.CO;2).
- Pope, S., 2000: *Turbulent Flows*. Cambridge University Press, 802 pp.
- Reichl, B. G., D. Wang, T. Hara, I. Ginis, and T. Kukulka, 2016: Langmuir turbulence parameterization in tropical cyclone conditions. *J. Phys. Oceanogr.*, **46**, 863–886, <https://doi.org/10.1175/JPO-D-15-0106.1>.
- Salesky, S. T., M. Chamecki, and E. Bou-Zeid, 2017: On the nature of the transition between roll and cellular organization in the convective boundary layer. *Bound.-Layer Meteor.*, **163**, 41–68, <https://doi.org/10.1007/s10546-016-0220-3>.
- Sinha, N., A. E. Tejada-Martínez, C. Akan, and C. E. Grosch, 2015: Toward a *K*-profile parameterization of Langmuir turbulence in shallow coastal shelves. *J. Phys. Oceanogr.*, **45**, 2869–2895, <https://doi.org/10.1175/JPO-D-14-0158.1>.
- Smyth, W. D., E. D. Skillingstad, G. B. Crawford, and H. Wijesekera, 2002: Nonlocal fluxes and Stokes drift effects in the *K*-profile parameterization. *Ocean Dyn.*, **52**, 104–115, <https://doi.org/10.1007/s10236-002-0012-9>.
- Sullivan, P. P., and J. C. McWilliams, 2010: Dynamics of winds and currents coupled to surface waves. *Annu. Rev. Fluid Mech.*, **42**, 19–42, <https://doi.org/10.1146/annurev-fluid-121108-145541>.
- Takaya, Y., J.-R. Bidlot, A. C. Beljaars, and P. A. Janssen, 2010: Refinements to a prognostic scheme of skin sea surface temperature. *J. Geophys. Res.*, **115**, C06009, <https://doi.org/10.1029/2009JC005985>.
- Taylor, G. I., 1922: Diffusion by continuous movements. *Proc. London Math. Soc.*, **s2-20**, 196–212, <https://doi.org/10.1112/plms/s2-20.1.196>.
- Thorpe, S., 2004: Langmuir circulation. *Annu. Rev. Fluid Mech.*, **36**, 55–79, <https://doi.org/10.1146/annurev.fluid.36.052203.071431>.
- Van Roekel, L., B. Fox-Kemper, P. Sullivan, P. Hamlington, and S. Haney, 2012: The form and orientation of Langmuir cells for misaligned winds and waves. *J. Geophys. Res.*, **117**, C05001, <https://doi.org/10.1029/2011JC007516>.
- , and Coauthors, 2018: The KPP boundary layer scheme for the ocean: Revisiting its formulation and benchmarking one-dimensional simulations relative to les. *J. Adv. Model. Earth Syst.*, **10**, 2647–2685, <https://doi.org/10.1029/2018MS001336>.
- Wyngaard, J. C., and R. A. Brost, 1984: Top-down and bottom-up diffusion of a scalar in the convective boundary layer. *J. Atmos. Sci.*, **41**, 102–112, [https://doi.org/10.1175/1520-0469\(1984\)041<0102:TDABUD>2.0.CO;2](https://doi.org/10.1175/1520-0469(1984)041<0102:TDABUD>2.0.CO;2).
- Yang, D., B. Chen, M. Chamecki, and C. Meneveau, 2015: Oil plumes and dispersion in Langmuir, upper-ocean turbulence: Large-eddy simulations and *K*-profile parameterization. *J. Geophys. Res. Oceans*, **120**, 4729–4759, <https://doi.org/10.1002/2014JC010542>.
- Zhou, B., S. Sun, K. Yao, and K. Zhu, 2018: Reexamining the gradient and countergradient representation of the local and nonlocal heat fluxes in the convective boundary layer. *J. Atmos. Sci.*, **75**, 2317–2336, <https://doi.org/10.1175/JAS-D-17-0198.1>.